Insights into the mechanism of intermediate-depth earthquakes from source properties as imaged by back projection of multiple seismic phases

E. Kiser,[1] M. Ishii,[1] C. H. Langmuir,[1] P. M. Shearer,[2] and H. Hirose[3]

Received 7 July 2010; revised 14 March 2011; accepted 6 April 2011; published 28 June 2011.

[1] This study investigates the spatial and temporal distribution of energy release of large, intermediate-depth earthquakes using a modified back projection technique first used to study the 2004 Sumatra-Andaman megathrust event. Multiple seismic phases are included in the back projection analysis, which provides the capability to determine the energy distribution with respect to depth and time. A total of 22 intermediate-depth earthquakes with moment magnitudes greater than or equal to 6.5 are investigated with hypocentral depths between 100 and 300 km. For most of these events, the vertical extent of energy release is either below the resolution of this study (≤5 km) or slightly above (≤15 km). This observation agrees with previous studies that find large, intermediate-depth earthquakes have subhorizontal rupture planes. The results also show a significant portion of the events have multiple rupture planes that are well separated in depth. The closeness in time of the ruptures on separate planes and the distance between the planes suggest dynamic triggering where the *P* waves from the first rupture initiate rupture on the second plane. We propose that a dehydration embrittlement mechanism combined with preferentially hydrated subhorizontal faults can explain the observations of dominant subhorizontal rupture planes and the frequent occurrence of rupture complexity involving multiple subevents.

Citation: Kiser, E., M. Ishii, C. H. Langmuir, P. M. Shearer, and H. Hirose (2011), Insights into the mechanism of intermediate-depth earthquakes from source properties as imaged by back projection of multiple seismic phases, *J. Geophys. Res.*, *116*, B06310, doi:10.1029/2010JB007831.

1. Introduction

[2] Deep earthquakes occur at pressure and temperature conditions which should prohibit brittle failure, and yet many of the rupture characteristics of deep earthquakes are similar to those of shallow events, such as double-couple focal mechanisms [*Frohlich*, 2006]. Traditionally, these earthquakes have been divided into two categories: intermediate-depth (60–300 km) and deep-focus (300–700 km) events [e.g., *Wadati*, 1929]. This classification is motivated by the bimodal distribution in the number of earthquakes with depth, where an exponential decrease in the number of earthquakes occurs from 60 km to about 300 km followed by an increase between 400 and 600 km which quickly drops off between 650 and 700 km [e.g., *Flinn and Engdahl*, 1965; *Frohlich*, 1989]. Studies of source characteristics (e.g., rupture complexity and aftershock productivity) and conditions within the subducting slab (e.g., stability of hydrous minerals) also broadly support this division of deep earthquakes [e.g., *Ringwood*, 1975; *Houston and Vidale*, 1994; *Persh and Houston*, 2004]. In this paper, we focus on the intermediate-depth earthquakes occurring at depths between 100 and 300 km.

[3] Many hypotheses have been proposed to explain the occurrence of intermediate-depth earthquakes, such as dehydration embrittlement and shear localization [e.g., *Raleigh and Paterson*, 1965; *Ogawa*, 1987; *Hobbs and Ord*, 1988; *Kirby et al.*, 1996; *Hacker et al.*, 2003; *Keleman and Hirth*, 2007]. In addition to work from the mineral physics community, these hypotheses are developed and tested based upon earthquake source studies. Over the past 25 to 30 years, the source processes of both deep and shallow events have most commonly been determined using waveform modeling [e.g., *Hartzell and Helmberger*, 1982; *Olsen and Apsel*, 1982; *Cohee and Beroza*, 1994; *Cotton and Campillo*, 1995; *Zeng and Anderson*, 1996; *Sekiguchi et al.*, 1996; *Antolik et al.*, 1999; *Ji et al.*, 2002; *Frankel*, 2004; *Rhie et al.*, 2007]. Though this method has been widely used, many studies have revealed limitations associated with *a priori* constraints required to stabilize the inversion [*Olsen and Apsel*, 1982; *Hartzell and Heaton*, 1983; *Beresnev*, 2003; *Lay et al.*, 2010; *Mai et al.*, 2007]. For example, one of the conditions used

[1]Department of Earth and Planetary Sciences, Harvard University, Cambridge, Massachusetts, USA.
[2]Institute of Geophysics and Planetary Physics, Scripps Institution of Oceanography, University of California, San Diego, La Jolla, California, USA.
[3]National Research Institute for Earth Science and Disaster Prevention, Tsukuba, Japan.

0148-0227/11/2010JB007831

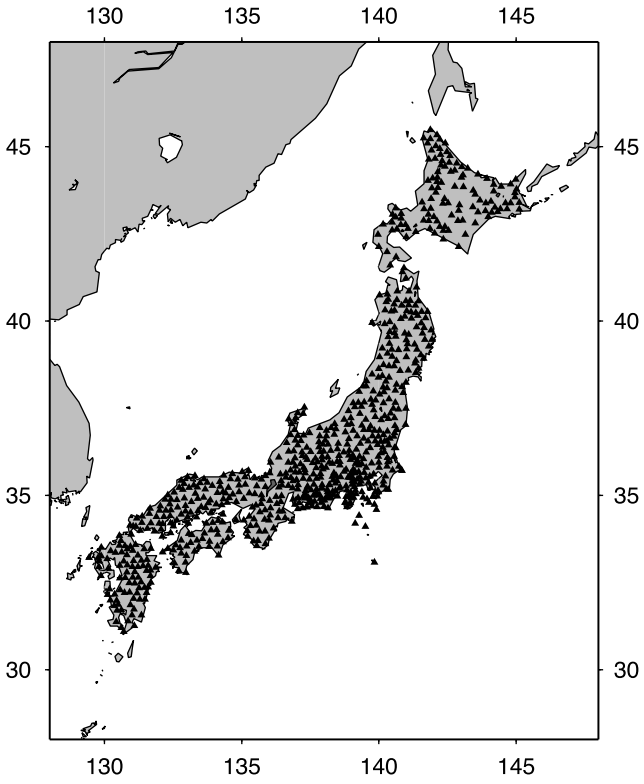

Figure 1. Distribution of the seismic stations (black triangles) in the High Sensitivity Seismograph Network (Hi-net) array throughout Japan. As of 27 February 2010 there were 776 stations.

in finite fault modeling is the fault plane geometry. Such constraints for shallow earthquakes are obtained based upon geologic studies or aftershock distributions [e.g., *Olsen and Apsel*, 1982]. For intermediate-depth earthquakes, however, there is no surface expression of the rupture and often very few aftershocks [e.g., *Frohlich*, 1987], making detailed estimates on the rupture plane dimensions and orientation difficult. Instead, waveforms are typically inverted onto one of the nodal planes from the focal mechanism [e.g., *Antolik et al.*, 1999]. This practice inherently limits the information that can be gained from source studies.

[4] The back projection technique used in this study is a more deterministic approach to studying earthquake rupture because it requires very little *a priori* knowledge. This approach has become feasible in recent years through the availability of high-quality data from large-aperture dense arrays such as the High-Sensitivity Seismograph Network (Hi-net; Figure 1) in Japan [*Okada et al.*, 2004; *Obara et al.*, 2005]. The application of the back projection method to a number of large earthquakes has shown that it is a quick and efficient way to determine some important properties of earthquake sources, such as total slip area, rupture direction, and rupture velocity [e.g., *Ishii et al.*, 2005, 2007; *Walker et al.*, 2005; *Walker and Shearer*, 2009; *Nelson et al.*, 2008; *Honda and Aoi*, 2009]. Previous studies of teleseismic events, however, analyzed data for the largest shallow earthquakes. In this manuscript, the back projection technique is modified to achieve good depth resolution to study the depth-time behavior of large (Mw $\geq$ 6.5) intermediate-depth earthquakes.

2. Method

[5] The back projection technique is similar to other methods that also utilize the time reversal property of seismic waves [e.g., *McMechan et al.*, 1985; *Reitbrock and Scherbaum*, 1994; *Ekström et al.*, 2003; *Kao and Shan*, 2004, 2007; *Baker et al.*, 2005; *MacAyeal et al.*, 2006; *Allmann and Shearer*, 2007; *Kao et al.*, 2008]. It was first used to study the 26 December 2004 Sumatra-Andaman earthquake [*Ishii et al.*, 2005], and has since been used to study many shallow earthquakes [e.g., *Ishii et al.*, 2005, 2007; *Walker et al.*, 2005; *Walker and Shearer*, 2009; *Nelson et al.*, 2008; *Honda and Aoi*, 2009].

[6] The back projection method time reverses seismograms from an array to a grid of potential source locations around the hypocenter using predicted travel times based upon a one-dimensional Earth model such as IASP91 [*Kennett*, 1991]. The seismograms are stacked at each grid point:

$$s_i(t) = \sum_{k=1}^{K} u_k(t - t_{ik}),$$

where $s_i(t)$ is the stacked seismogram at the ith grid point, $u_k(t)$ is the seismogram recorded at the kth station, t_{ik} is the predicted travel time between grid i and station k, and K is the total number of recorded seismograms. The grid points in this study are set up in three dimensions around the hypocenter, which makes it possible to study earthquake sources with respect to depth and lateral space.

[7] The one-dimensional Earth model does not include lateral variations which can produce deviations from the theoretical travel times. To correct for these lateral variations, we cross correlate the initial few seconds of the *P* waveforms between stations within the array and align the waveforms [*Ishii et al.*, 2007]. This process empirically corrects for the lateral variations, and ensures a coherent stack at the hypocenter. The cross correlation also provides amplitude and polarity information for each seismogram with respect to a reference waveform. Including this information modifies the expression for the stacks to

$$s_i(t) = \sum_{k=1}^{K} \alpha_k \, u_k(t - t_{ik} + \Delta t_k).$$

Here, Δt_k is the empirical time correction for each station obtained from the cross correlation procedure, and α_k is a weighting factor to ensure proper polarity and contribution from each trace. α_k can be defined to consider various effects such as array geometry [e.g., *Ishii et al.*, 2007], but the simplest form is

$$\alpha_k = \frac{p_k}{A_k},$$

where p_k is the polarity and A_k is an amplitude factor for seismogram k. The factor p_k has a value of either 1 or -1. The amplitude factor A_k obtained during the cross correlation step normalizes all of the seismograms so that a small group of

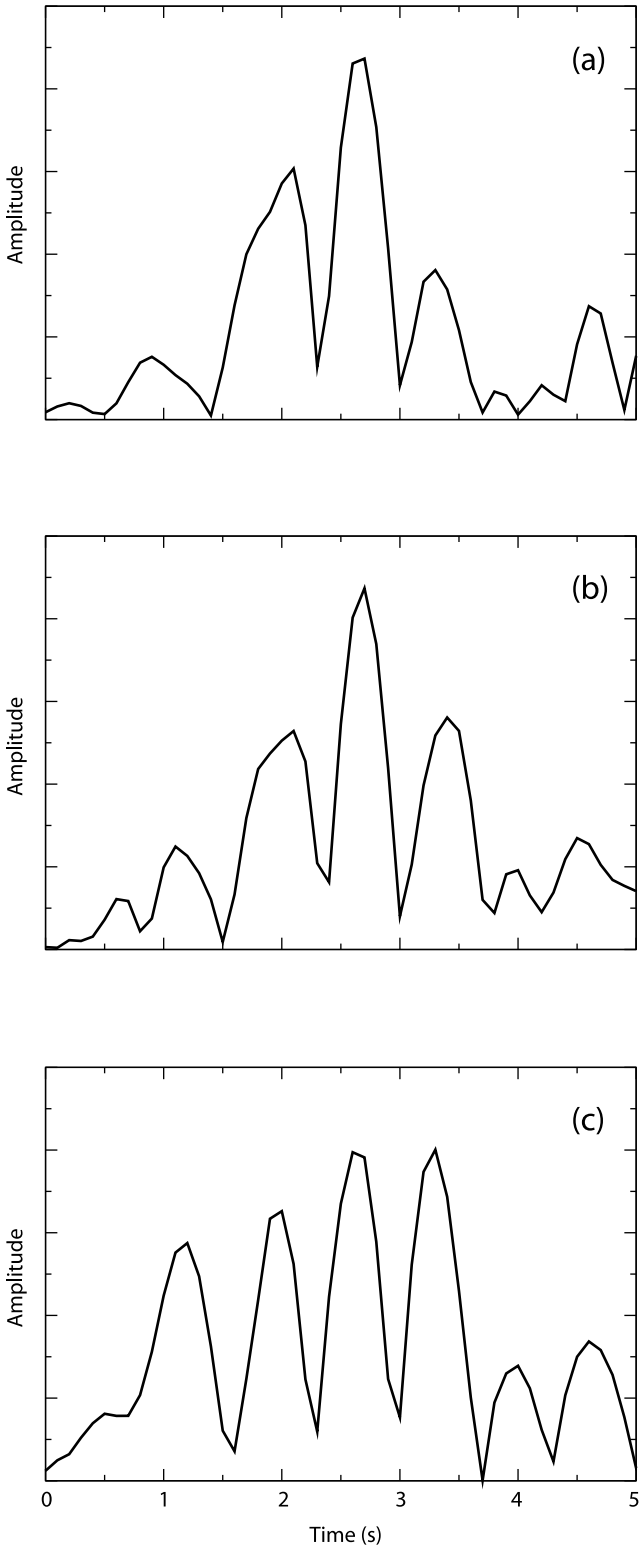

Figure 2. The absolute amplitudes of the first 5 s of stacks from three seismic phases, (a) *P*, (b) *pP*, and (c) *sP*, at the hypocenter after the time shifts (Δt_j) have been applied. These stacks are from the 8 September 2008, Mw 6.9 earthquake. Times are with respect to the hypocentral time.

high amplitude seismograms do not dominate the stacking process.

[8] We have expanded the above basic back projection technique to include additional seismic wave arrivals. The use of multiple seismic phases can improve resolution, espe-

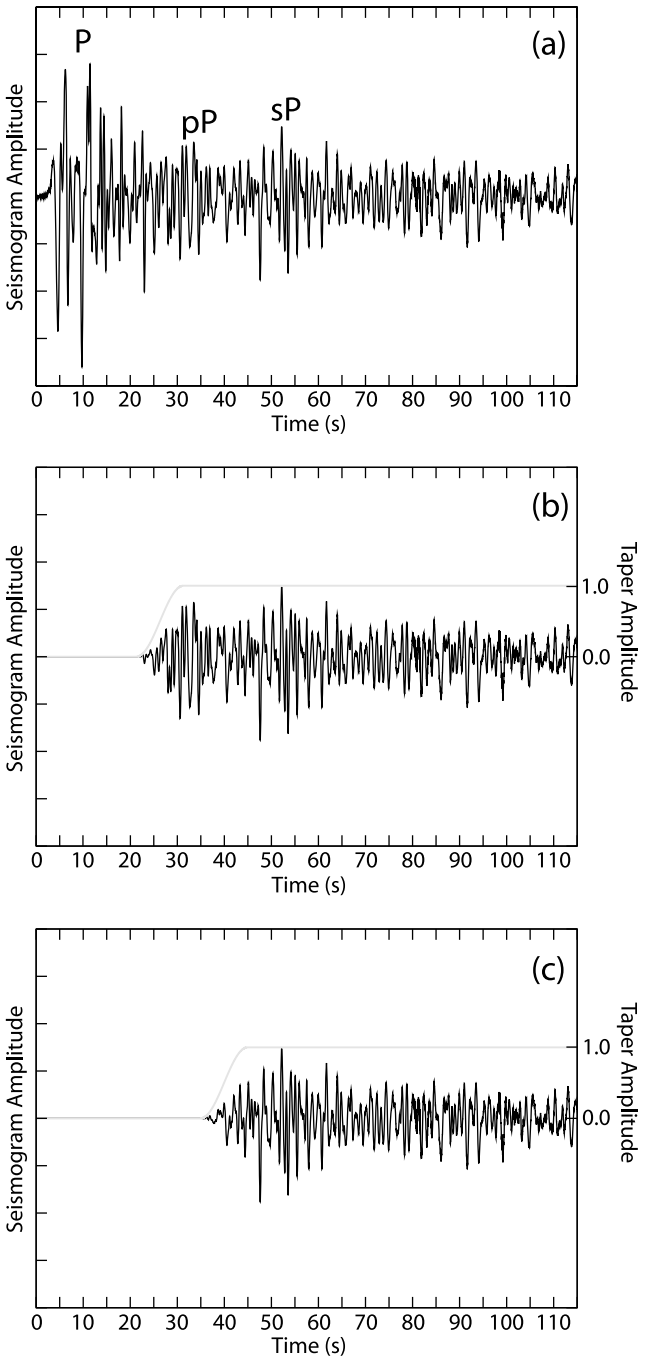

Figure 3. Effect of the taper function. (a) Seismic record from the 8 September 2008, Mw 6.9 event in Vanuatu. This record comes from station ASHH in the Hi-net array. The *P*, *pP*, and *sP* seismic phases are all labeled. Time is with respect to the theoretical *P* wave arrival. (b) The same seismic record after the taper function (light grey line) is applied at the theoretical *pP* arrival time. (c) Same as Figure 3b except applied to *sP*.

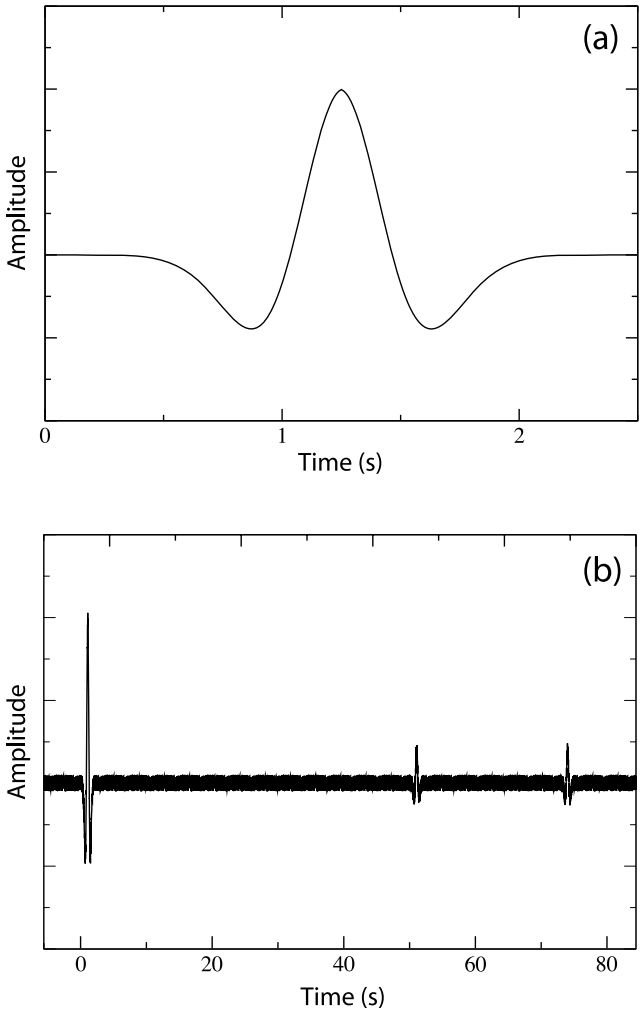

Figure 4. Synthetic seismogram. (a) A Ricker wavelet. (b) Example synthetic seismogram at station TBTH from a source at 13.50°S, 166.97°E, and 110 km depth. Time is with respect to the *P* wave arrival and noise is included with amplitude that is 10% of the input *P* wave.

cially with respect to depth if depth phases are included, as demonstrated in subsequent sections. The seismograms are stacked for each phase based upon the predicted travel time and the time correction Δt_k obtained for the reference phase. The stacks from multiple phases are combined such that

$$s_i(t) = \sum_{j=1}^{J} \left| \sum_{k=1}^{K} \alpha_k \, u_k\left(t - t_{ik}^j + \Delta t_k\right) \right|,$$

where J is the total number of seismic phases used, and t_{ik}^j is the predicted travel time for the jth seismic phase between the ith grid point and the kth station.

[9] A few additional steps are taken to reduce unwanted signal and to enhance coherency between phase stacks. For example, the *P* wave for a relatively shallow earthquake arrives close to the depth phase *pP*, and its amplitude is typically much larger than the depth phase. The slownesses of the two phases are also similar enough that back projection using the depth phase arrival times will result in the depth phase stack that includes large amplitude signals due to the *P* wave arrival. In order to suppress such signals, a taper function $f_{jk}(t)$ is used to eliminate arrivals before the target phase. The taper function $f_{jk}(t)$ is defined as

$$f_{jk}(t) = \begin{cases} 0 & \text{for} \quad t \le t_{0k}^j - T/2 \\ \frac{1}{2}\left\{\cos\left[\frac{2\left(t - t_{0k}^j\right)\pi}{T}\right] + 1\right\} & \text{for} \quad t_{0k}^j - T/2 < t < t_{0k}^j \\ 1 & \text{for} \quad t \ge t_{0k}^j \end{cases},$$

where t_{0k}^j is the predicted travel time of the jth phase to the kth station from the hypocenter, and T is the period of the cosine taper function that is prescribed.

[10] Another step taken when combining seismic phases is to apply an additional weighting factor (w_j) to the stacks of each seismic phase, so that one phase does not dominate the final result. The weighting factor (w_j) can be expressed in many different ways, with the most basic form being

$$w_j = \frac{A_{ref}^{\max}}{A_j^{\max}}.$$

Here, $A_{ref}^{\max}$ is the maximum amplitude of the reference phase stacks and $A_j^{\max}$ is the maximum amplitude of the stacks of the jth phase being considered. If a majority of the phases have upward or downward takeoff directions, there will be a bias in the contribution to back projected stacks if the above weighting factor is used. For example, when *P*, *pP*, and *sP* are used in the back projection analysis, there will be a bias in the upward takeoff direction. We therefore modify the weighting factor for the depth phases to

$$w_j = \frac{c_j}{\sum_{l=2}^{J} c_l} \frac{A_{ref}^{\max}}{A_j^{\max}},$$

where c_j is the maximum correlation coefficient between the reference stack and the jth depth phase stack at the hypocenter. The summation in the denominator begins at 2 because this weighting factor is not being applied to the *P* phase. The above formulations are based upon maximum stack amplitudes. Alternatively, one can use the ratio of summed stacks or the amplitude information from a hypocentral stack cross correlation. We have investigated both of these approaches without any significant changes to the final results.

[11] Finally, we apply the constraint that the stacks from different seismic phases sum coherently at the hypocenter. To accomplish this, a second empirical time shift (Δt_j) is obtained by cross correlating the different phase stacks against a reference phase stack at the hypocenter (Figure 2). Including these additional steps modifies the expression for the stacks at each grid point to

$$s_i(t) = \sum_{j=1}^{J} w_j \left| \sum_{k=1}^{K} f_{jk}(t)\, \alpha_k \, u_k\left(t - t_{ik}^j + \Delta t_k + \Delta t_j\right) \right|.$$

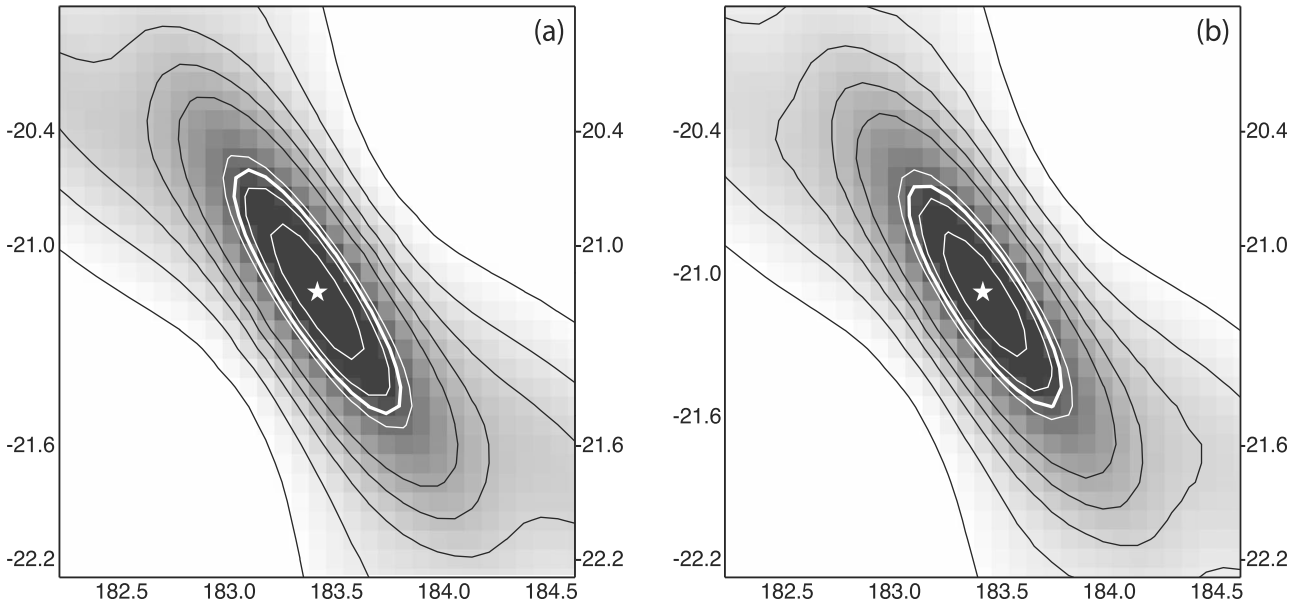

Figure 5. Lateral resolution. (a) Map view of the synthetic back projection result using only *P* waves from a point source at 21.08°S, 176.59°W, and 212 km depth. The white star is the location of the point source, the thin black and white lines are 10% contours of the integrated squared stack amplitudes, and the thick white line is the 75% contour curve used in subsequent figures to estimate the regions of slip. The background colors indicate high (black) and low (white) stack amplitudes. (b) Map view of the same back projection result as in Figure 5a, but using the *P*, *pP*, and *sP* phases.

The stacks $s_i(t)$ give time and relative amplitude information of energy released by an earthquake, providing constraints on the rupture process.

3. Data and Data Processing

[12] Implementation of the High-Sensitivity Seismograph Network (Hi-net) in Japan began after the Kobe earthquake in 1995, and data from the array have been available since October 2000 [*Okada et al.*, 2004; *Obara et al.*, 2005]. There are currently around 800 stations in this array with a targeted station spacing of 20 km (Figure 1). Borehole short-period instruments (100 samples/s) are placed around 100 m depth. These sites are recording 3 components of ground motion, though only the vertical component is used in this study. Three phases are used in the back projection analysis: *P*, *pP*, and *sP*. As the subsequent section will show, the difference in takeoff direction between *P* and the depth phases, *pP* and *sP*, produces very good depth resolution when all three phases are combined.

[13] In order to obtain the empirical correction for lateral variations in the velocity structure of the Earth, Δt_k, a cross correlation analysis is applied to *P* waves. The waveforms are cross correlated in a 4 s time window, which is allowed to shift by ±2 s, around the predicted arrival times based upon the one-dimensional velocity model IASP91 [*Kennett and Engdahl*, 1991]. A cluster analysis is applied [e.g., *Romesburg*, 1984] to identify the largest group of seismograms with high waveform similarity to generate the first reference stack. This reference stack is then cross correlated with each seismogram, as in the first step, and those with a correlation coefficient above 0.6 are stacked to produce the second reference stack. This step is repeated five times to generate a final reference stack. Each seismogram is then correlated with this final reference stack to obtain the polarity (p_k), the amplitude factor (A_k), and the relative time shift (Δt_k). Only the first arriving *P* waves are cross correlated and the same time shifts are used to correct every seismic phase considered. The cross correlation technique can be applied to any individual seismic phase, but the depth phases (*pP* and *sP*) considered in this study typically have low signal-to-noise ratios, making the cross correlation procedure less effective.

[14] The low signal-to-noise ratios of the depth phases compared to the *P* phase also demonstrate the necessity for using the taper function $f_{jk}(t)$. The taper function prevents the high amplitude *P* waves from contaminating the depth phase stacks (Figure 3). The period *T* over which the taper function goes from 1 to 0 is fixed at 10 s. Varying this value has little effect on the final results as long as it is a short enough time window to down weight the *P* waves and long enough to avoid generating artifacts due to an abrupt cutoff. The taper function can also suppress signals from the depth phases if these phases arrive significantly before the theoretical times. This possibility is evaluated by shifting the taper function gradually up to 5 s before the theoretical arrival time and monitoring the correlation coefficients between the *P* stack and depth phase stacks at the hypocenter. If the depth phase signal arrives earlier than predicted, then the shifted taper function should allow more of the depth phase signal to be present in the depth phase stacks. This would increase the correlation coefficient between the stacks at the hypocenter. In contrast, if the depth phase arrives at, or later than, the predicted time, then only noise and the *P* waveform is down weighted by the original taper function, leading to a lower correlation coefficient using the shifted taper function. Seven

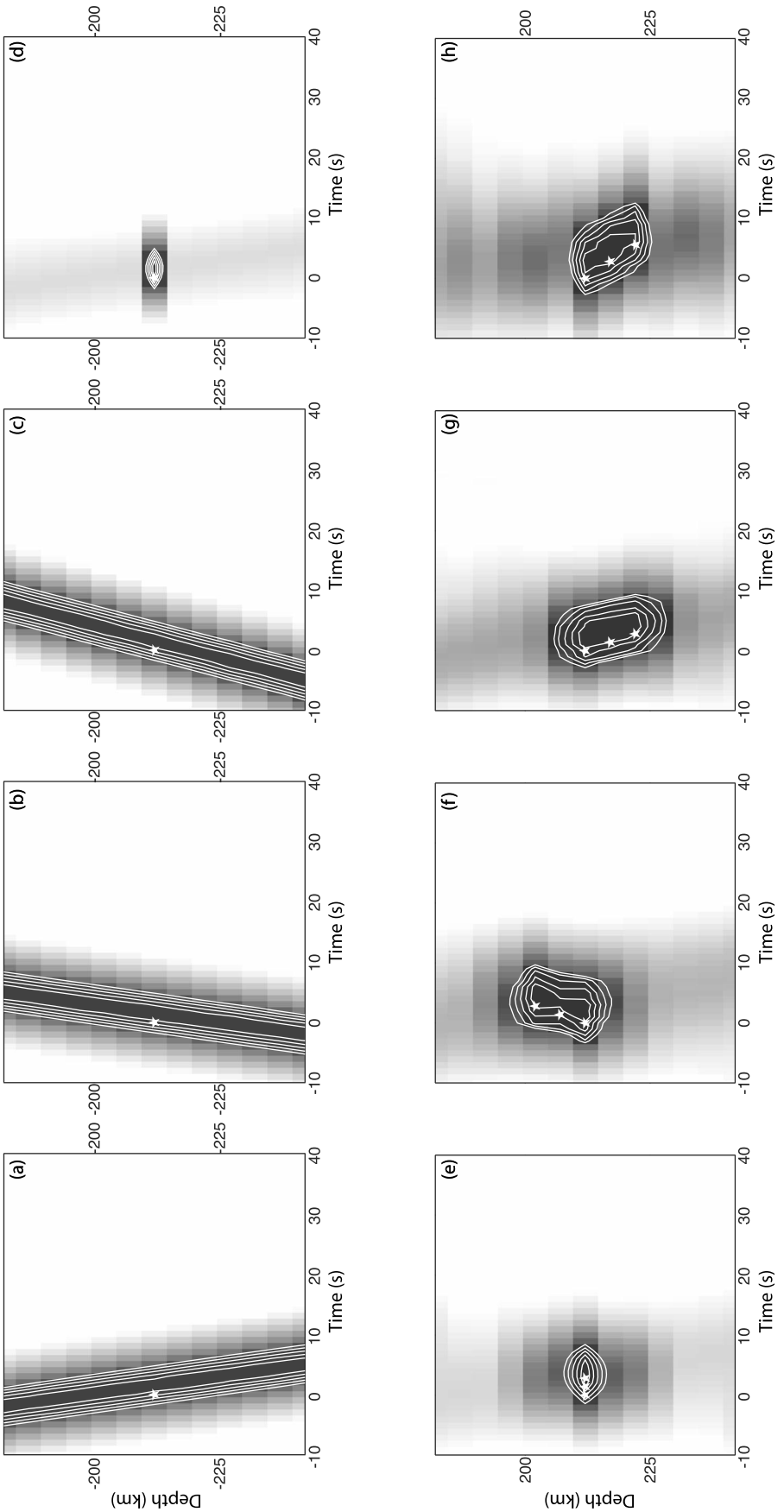

Figure 6

Table 1. Summary of the Tonga-Kermadec Events Analyzed With the Back Projection Technique and the Hi-net Data in Japan[a]

Date and Time	Latitude	Longitude	Depth	Mw	Number of Ruptures	Rupture Depth	Vertical Extent	Event Duration	Cumulative Duration	Phases Used	ϵ	Figure
06/03/01 02:41:57	−29.67	−178.63	178	7.2	1	178	−20 +5	14	14	pP,sP	−0.05	8f
07/04/01 07:06:31	−21.73	−176.71	184	6.5	1	184	0	12	12	pP,sP	0.10	8e
07/27/03 02:04:11	−21.08	−176.59	212	6.6	1	212	−5 +10	14	14	pP,sP	−0.07	8a
01/25/04 11:43:11	−16.83	−174.20	129	6.7	1	129	+5	13	13	sP	0.13	8d
05/16/06 10:39:23	−31.81	−179.31	153	7.4	2	153; 178	+15; 0	15	22	pP,sP	0.16	8c
12/09/07 07:28:20	−26.00	−177.51	157	7.8	2	157; 187	0; −5	16	26	pP,sP	−0.25	8b

[a]The first five columns give hypocentral date and time (UTC), latitude, longitude, depth, and moment magnitude, obtained from the National Earthquake Information Center (http://earthquake.usgs.gov/regional/neic/). The column "Number of Ruptures" gives the number of subevents with a minimum of 15 km depth separation as described in the main text. For each subevent, the depth at its initiation is given in the "Rupture Depth" column. The depth extent for each subevent is resolved with the technique presented in this paper, and they are summarized in the "Vertical Extent" column, with the value given in increments of 5 km, and the sign indicating the direction, i.e., positive for downward propagation and negative for upward propagation. Subevents with both positive and negative entries indicate bivertical rupture. The following two columns give duration information inferred from the back projection results. The "Event Duration" is the duration of the entire event. In contrast, the "Cumulative Duration" gives the sum of the durations of subevents. Large differences between these two values indicate that there is significant overlap of the subevent ruptures in time. The "Phases Used" column shows the depth phases that have been combined with the *P* wave stacks. In most cases, both *pP* and *sP* phases are used, except when the source mechanism is such that *pP* is not excited well. The next to last column gives the ϵ value that represents the non-double-couple component of the event (see main text for definition). The final column gives the corresponding back projection plot for each earthquake. Note that on average, the uncertainties in depth and time are ±5 km and ±5.0 s, respectively.

of the events have correlation coefficients for one of the depth phases that become larger when the shifted taper function is used, and therefore we choose to apply the shifted taper function in the back projection analysis for these cases. However, in general, shifting the taper function has little effect on the back projection results.

[15] As discussed in the previous section, the form of the weighting factor for each phase w_j can change depending on the seismic phases being used. There are five earthquakes for which one of the depth phases is predicted to have an amplitude much smaller than the *P* phase (10% or less) based upon Global CMT solutions [e.g., *Dziewonski et al.*, 1981; *Dziewonski and Woodhouse*, 1983; *Woodhouse and Dziewonski*, 1984; *Ekström et al.*, 2005]. For these events, only the higher amplitude depth phase is used with weighting specified by the basic weighting factor. Finally, the phase-dependent time shift (Δt_j) is obtained by cross correlating the depth phase stacks at the hypocenter with the hypocentral *P* stack.

4. Synthetic Tests

[16] In order to interpret results of this method, it is essential to understand how different steps described in the previous sections influence the final results. In general, we investigate artifacts of the technique by applying the back projection method to synthetic seismograms to determine how well the input source parameters are recovered. Synthetic seismographs are generated using a simple Ricker wavelet [*Ricker*, 1953, Figure 4a] with central frequency of

Figure 6. Depth-time resolution. The white stars are the depths and times of the point sources, and the white lines are 5% contours between 75% and 100% of the maximum value of the squared stack. Time is with respect to the hypocentral time and the background colors indicate high (black) and low (white) stack amplitudes. These plots are made by first creating comprehensive stacks at each depth by selecting the maximum stack amplitude at each time from all of the grid points at a particular depth. Following this, the squared amplitudes of the depth stacks are integrated in 10 s windows. The time interval is 1 s. (a) Synthetic back projection result of a point source located at 21.08°S, 176.59°W, and 212 km depth using only the *P* phase. Time is with respect to the hypocentral time and the background colors indicate high (black) and low (white) stack amplitudes. (b) Same as in Figure 6a except for results using only the *pP* phase. (c) Same as in Figure 6a except for results using only the *sP* phase. (d) Synthetic back projection result using all three seismic phases. (e) Synthetic result from three point sources (white stars) separated laterally and in time. This arrangement is meant to simulate a horizontal rupture plane. The three point sources are each separated by 5 km to the east and 1.4 s in time. This leads to a rupture velocity of 3.6 km/s in the horizontal direction. The result is obtained by using all three seismic phases considered in this study. (f) Synthetic result from three point sources (white stars) separated in depth and time using all three phases. This arrangement is meant to simulate a vertical plane with rupture propagation upward. The three point sources are each separated by 5 km in depth and 1.4 s in time, but have the same latitude and longitude. This leads to a rupture velocity of 3.6 km/s in the vertical direction. (g) Same as in Figure 6f except with propagation downward. (h) Synthetic result from three point sources (white stars) separated in longitude, depth, and time using all three seismic phases. This arrangement is meant to simulate a rupture dipping at 30 degrees. The three point sources are each separated by 8.7 km to the east, 5 km in depth, and 2.8 s in time. This setup is used so that the vertical extent (10 km) and rupture velocity (3.6 km/s) are the same as in Figure 6g.

Table 2. Summary of the Vanuatu Events Analyzed With the Back Projection Technique and the Hi-net Data in Japan.

Date and Time	Latitude	Longitude	Depth	Mw	Number of Ruptures	Rupture Depth	Vertical Extent	Event Duration	Cumulative Duration	Phases Used	ϵ	Figure
01/09/01 16:49:28	−14.93	167.17	103	7.1	1	103	0	14	14	pP,sP	0.11	9c
11/06/03 10:38:04	−19.26	168.89	113	6.6	2	113; 138	−5; +10	14	22	pP,sP	−0.29	9h
04/09/04 15:23:35	−13.17	167.20	228	6.5	1	228	−10	14 +5	14	pP,sP	0.10	9e
02/08/05 14:48:21	−14.25	167.26	206	6.7	1	206	0	14	14	pP,sP	0.03	9b
08/07/06 22:18:55	−15.80	167.79	149	6.8	3	149; 179; 224	−15 +15; −10; 0	19	25	pP,sP	0.22	9d
08/01/07 17:08:51	−15.60	167.68	120	7.2	1	120	0	14	14	pP,sP	−0.01	9g
09/08/08 18:52:06	−13.50	166.97	110	6.9	1	110	0	14	14	pP,sP	0.13	9a
03/04/10 14:02:27	−13.60	167.16	176	6.5	1	176	+5	15	15	pP,sP	0.03	9f

Table 3. Summary of the Hindu Kush Events Analyzed With the Back Projection Technique and the Hi-net Data in Japan

Date and Time	Latitude	Longitude	Depth	Mw	Number of Ruptures	Rupture Depth	Vertical Extent	Event Duration	Cumulative Duration	Phases Used	ϵ	Figure
03/03/02 12:08:19	36.50	70.48	225	7.4	2	225; 300	−15 +10; +5	21	27	sP	0.03	10a
04/05/04 21:24:04	36.51	71.03	187	6.6	1	187	−10 +5	13	13	pP,sP	0.01	10c
12/12/05 21:47:46	36.36	71.09	230	6.5	1	230	−10 +15	15	15	pP,sP	−0.04	10d
01/03/09 20:23:20	36.42	70.74	204	6.6	1	204	−10 +20	14	14	sP	0.09	10b

Table 4. Summary of the Java Events Analyzed With the Back Projection Technique and the Hi-net Data in Japan

Date and Time	Latitude	Longitude	Depth	Mw	Number of Ruptures	Rupture Depth	Vertical Extent	Event Duration	Cumulative Duration	Phases Used	ϵ	Figure
03/02/05 10:42:12	−6.53	129.93	191	7.1	2	191; 221	−10 +15; 0	13	19	pP,sP	0.00	11b
08/08/07 17:05:04	−5.86	107.42	280	7.5	1	280	−5	9 +30	9	pP,sP	0.08	11a
10/24/09 14:40:43	−6.13	130.38	138	6.9	2	138; 168	−10 +10; −5	12	17	pP,sP	0.27	11c

Table 5. Summary of the Alaska Events Analyzed With the Back Projection Technique and the Hi-net Data in Japan

Date and Time	Latitude	Longitude	Depth	Mw	Number of Ruptures	Rupture Depth	Vertical Extent	Event Duration	Cumulative Duration	Phases Used	ϵ	Figure
07/28/01 07:32:43	59.03	−155.12	131	6.8	2	131; 161	−10; −10 +5	9	15	sP	−0.03	12

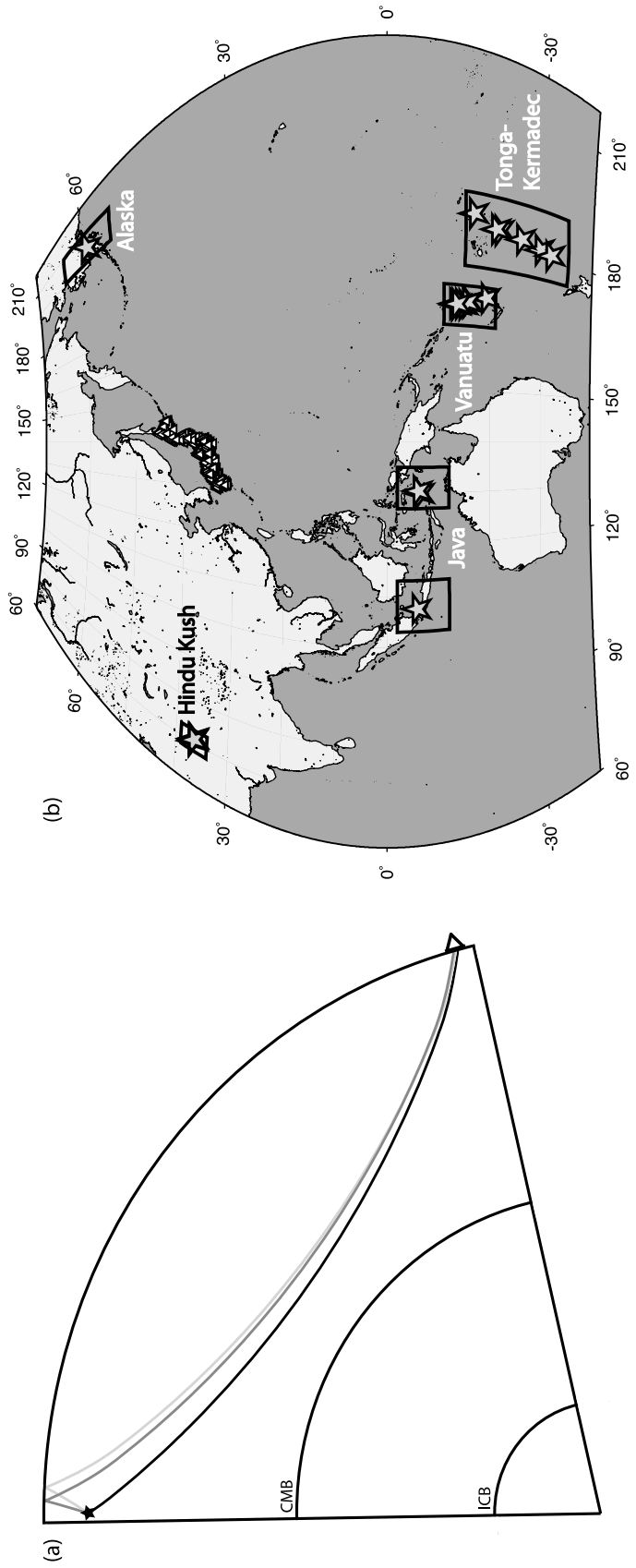

Figure 7. Seismic phases and distribution of intermediate-depth earthquakes studied in this paper. (a) The raypaths of the *P* (black line), *pP* (dark grey), and *sP* (light grey) phases from the source (star) to the receiver (triangle). The difference in the takeoff directions between the *P* phase and depth phases (*pP* and *sP*) results in excellent vertical resolution when stacks from each phase are combined. (b) Locations of the 22 earthquakes studied (grey stars) relative to the Hi-net array (white triangles). The black boxes are the areas displayed in Figures 8–12.

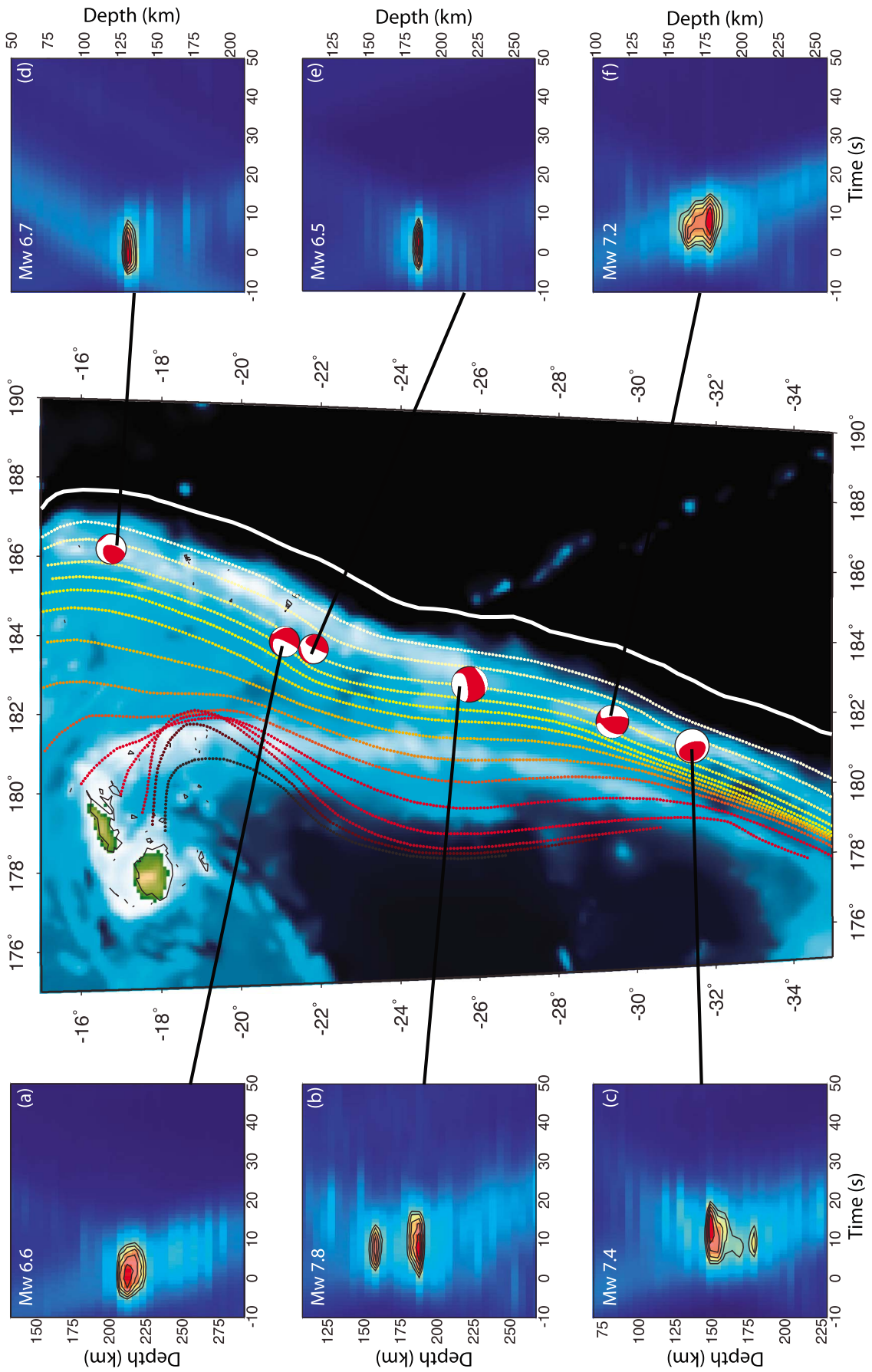
(a)
Mw 6.6
(b)
Mw 7.8
(c)
Mw 7.4
(d)
Mw 6.7
(e)
Mw 6.5
(f)
Mw 7.2
Depth (km)
Time (s)
176°
178°
180°
182°
184°
186°
188°
190°
-16°
-18°
-20°
-22°
-24°
-26°
-28°
-30°
-32°
-34°

Figure 8

1.0 Hz from a point source. The arrival times of the wavelets are determined for all stations in the Hi-net array using a one-dimensional velocity model of the Earth for a given source location (Figure 4b). This is done for all three seismic phases (*P*, *pP*, and *sP*).

4.1. Lateral Resolution

[17] A similar approach has been used to determine the lateral resolution in previous studies [e.g., *Ishii et al.*, 2007]. These studies show that poor lateral resolution is caused by the imperfect azimuthal and distance coverage of the data being used. Figure 5a shows the back projection result for a single point source using only the *P* phase. The limited azimuthal coverage of the Hi-net array leads to substantial lateral smearing. The amount of smearing varies greatly depending on the direction, the energy contour being used, and the array geometry with respect to the source location. For this study, the 75% contour is used to estimate the slip region. Using the same contour, a point source is broadened to an area of 3700 km^2. Improvements to the lateral resolution using multiple seismic phases are minimal with an area of 3300 km^2 inside the 75% contour (Figure 5b). As this synthetic test shows, lateral resolution is poor, and only the details of very large earthquakes can be obtained in these dimensions. For example, estimates of the minimum magnitude required for reliable constraints on horizontal properties, such as lateral rupture propagation, is Mw 7.4 in the Sumatra region using the Hi-net data [*Ishii et al.*, 2007], and most of the events considered in this study are smaller than this threshold.

4.2. Depth and Time Resolution

[18] To illustrate the depth and time resolution, Figure 6 compares the depth-time distribution of imaged energy from synthetic tests using individual phases, as well as combinations of phases. These results show that back projection of a single phase provides no depth resolution. The smearing in these cases is along the raypaths of the different phases (Figures 6a, 6b, and 6c). However, if the *P* phase is combined with one or both of the depth phases, the depth resolution improves dramatically to approximately ±5 km (Figure 6d). This uncertainty is valid for all earthquake locations considered in this study. The time resolution (±5 s) is also very consistent between different source locations. These tests show that results are most reliable in depth and time, hence we focus our discussion and interpretation of the earthquakes in these two dimensions.

4.3. Synthetic Ruptures in Depth and Time

[19] In addition to determining the resolution of a point source, it is critical to understand how well back projection can image an earthquake rupture and the appearance of this rupture in the depth-time projection we have chosen. To address this, multiple point sources separated in space and time are used to simulate a propagating rupture. Figures 6e–6h show results of four synthetic tests. For all four of these synthetic tests, the locations and times of the three point sources are assigned to simulate a rupture velocity of 3.6 km/s (80% of the shear wave speed [*Kennett and Engdahl*, 1991]). The horizontal rupture result in Figure 6e shows that this rupture looks similar to a point source result, however, the duration reflects the input source duration. The two vertical ruptures in Figures 6f and 6g show that back projection can recover a rupture that propagates upward or downward. Finally, Figure 6h shows the back projection result for a synthetic rupture that has the same rupture depth extent as Figure 6g, but the dip has been changed to 30 degrees. This result shows that if the rupture velocity is constant, we should be able to at least qualitatively recognize differences in the rupture plane dips. Though these synthetic results all have eastward propagating ruptures and common depth extents, the resolution of imaged energy is the same when these parameters are changed (Figure S1 of the auxiliary material).[1]

[20] An important feature to note is the locations of low amplitude energy for the horizontal and subhorizontal synthetic ruptures (Figures 6e and 6h). In both cases the energy, which falls below the 75 % contour, occurs symmetrically above and below the high amplitude stacks. This is an artifact of the *P* phase from one point source combining with the depth phase from a different point source. Though these artifacts are low amplitude, they show that symmetric rupture patterns should be met with some degree of skepticism.

5. Results

[21] The multiphase back projection analysis is applied to 22 intermediate-depth earthquakes (Tables 1–5 and Figure 7). These events occurred between October 2000 and April 2010, and were at teleseismic distances from the Hi-net array. The moment magnitudes and depths of these events, as reported by the USGS (http://earthquake.usgs.gov/regional/neic/), range from 6.5 to 7.8 and 103 to 280 km, respectively. For all of these

[1] Auxiliary materials are available in the HTML. doi:10.1029/2010JB007831.

Figure 8. Tonga-Kermadec earthquakes. This plot shows locations, focal mechanisms from the Global CMT catalogue [e.g., *Dziewonski et al.*, 1981; *Dziewonski and Woodhouse*, 1983; *Woodhouse and Dziewonski*, 1984; *Ekström et al.*, 2005], and the back projection results of the earthquakes studied in the Tonga-Kermadec region. The map in the center shows the region with background color showing the bathymetry (ETOPO5; http://www.ngdc.noaa.gov/mgg/global/etopo5.html). The solid white line is the trench location. The dotted lines are the slab contours from 50 to 700 km (white to dark red) in 50 km increments. Figures 8a–8f show the back projection results in the depth and time dimensions. The magnitudes and hypocentral depths are from the National Earthquake Information Center (NEIC) catalog (http://earthquake.usgs.gov/regional/neic/). The background colors indicate high (dark red) and low (dark blue) stack amplitudes. See Table 1 for a summary of the results. (a) The 27 July 2003 event with magnitude Mw 6.6 at a depth of 212 km. (b) The 9 December 2007 event with magnitude Mw 7.8 at a depth of 152 km. (c) The 16 May 2006 event with magnitude Mw 7.4 at a depth of 152 km. (d) The 25 January 2004 event with magnitude Mw 6.7 at a depth of 129 km. (e) The 4 July 2001 event with magnitude Mw 6.5 at a depth of 184 km. (f) The 3 June 2001 event with magnitude Mw 7.2 at a depth of 178 km.

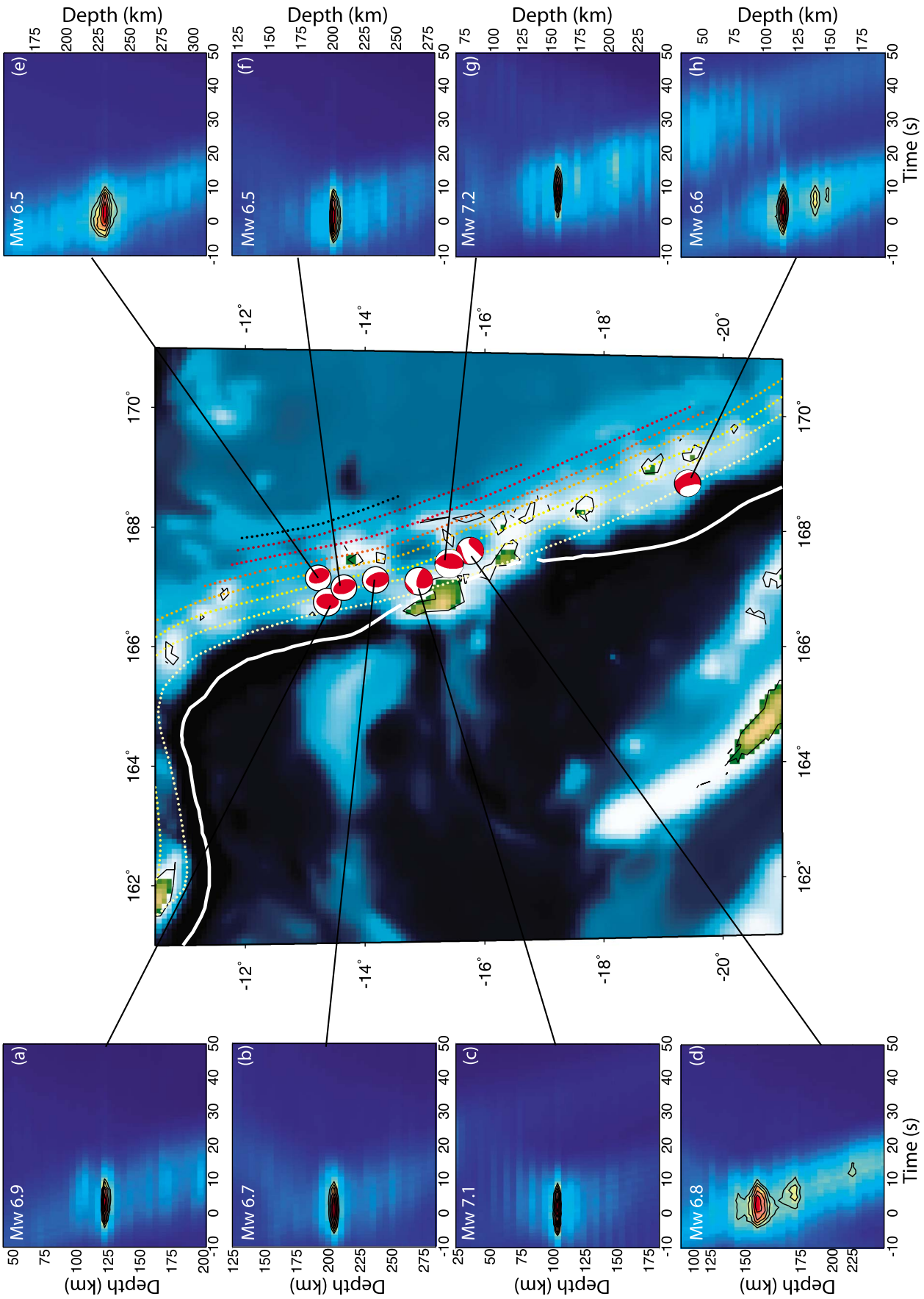
(a)
Mw 6.9
(b)
Mw 6.7
(c)
Mw 7.1
(d)
Mw 6.8
(e)
Mw 6.5
(f)
Mw 6.5
(g)
Mw 7.2
(h)
Mw 6.6
Depth (km)
Time (s)
162°
164°
166°
168°
170°
-12°
-14°
-16°
-18°
-20°

Figure 9

earthquakes, a box of grid points centered at the hypocenter is defined with dimensions of 2.4 degrees in latitude, 2.4 degrees in longitude, and 160 km in depth. The grid spacing, which is based upon the average resolution in latitude, longitude, and depth, is set to 0.4 degrees, 0.4 degrees, and 5 km, respectively. We choose the 75% contour of the maximum stack amplitude to estimate the depth extent and duration of each event (Tables 1–5). This choice is somewhat arbitrary, however, it seems to capture the major features for most of the earthquakes. Using this contour level, many of the events (14 out of 22) show similar depth-time behavior to the synthetic ruptures in the previous section in that they have one episode of energy release that is continuous in depth and time. The remaining 8 earthquakes have multiple regions of high amplitude energy that are well separated in time and/or depth. In order to systematically categorize events consisting of a single or multiple subevents, we use the selection criterion that the initiation depths of the subevents need to be separated by at least 15 km. When this criterion is met, we refer to the event as composite. When the depth separation is less than 15 km, the events are labeled simple. In addition, the observed depth extent of individual subevents can be classified into two groups, one with limited depth range and another showing energy release over a much larger depth interval. Most of the subevents are of the first group, with 23 out of 30 subevents having depth extents of 15 km or less (Tables 1–5). We refer to these subevents as subhorizontal ruptures. In the following sections, we discuss results for events in each region shown in Figure 7.

5.1. Tonga-Kermadec

[22] The Tonga-Kermadec trench subducts the 70–100 Myr old Pacific plate beneath the Indo-Australian Plate at a rate which increases to the north from rates of 16 to 24 cm/yr [*Bevis et al.*, 1995]. The hypocentral depths of six events in this region range from 129 to 212 km, and their moment magnitudes vary between 6.5 and 7.8 (http://earthquake.usgs.gov/regional/neic/) (Figure 8). Four of the events are interpreted as simple ruptures (Figures 8a, 8d, 8e, and 8f). The depth extent of these events varies from 0 km to 25 km, and their durations range from 12 to 14 s (Table 1). The remaining 2 earthquakes are composite events, with two subevents separated in depth by 25 and 30 km (Figures 8b and 8c, respectively). The event duration of these composite events is slightly longer than the simple events, 15 to 16 s (Table 1).

5.2. Vanuatu

[23] Along the Vanuatu subduction zone, the Indo-Australian plate is subducting beneath the Pacific plate. There are large variations in the subduction rates along the trench, ranging from 3 cm/yr to 17 cm/yr [e.g., *Bergeot et al.*, 2009]. Figure 9 shows the regional distribution of earthquakes and the back projection results. These events have magnitudes and depths that range from 6.5 to 7.2 and 103 to 228 km, respectively (http://earthquake.usgs.gov/regional/neic/). Five of the earthquakes from Vanuatu have simple ruptures with depth extents of 5 km or less (Figures 9a, 9b, 9c, 9f, and 9g). The duration of these events ranges from 14 to 15 s. The 1 August 2007, Mw 7.2 event (Figure 9g) from this group seems to have complexity beyond the single rupture, however, all of this complexity is weak, at energy levels below the 75% contour. The northernmost and deepest event from this region also has a single rupture which propagates upward and downward with time (Figure 9e), though the upward propagation dominates. South of these simple events are two composite events. The 7 August 2006, Mw 6.8 earthquake is composed of 3 subevents (Figure 9d). The largest depth separation between any two of these subevents is 75 km. The second composite event (Mw 6.6) occurred on 6 November 2003 (Figure 9h). Two features of this earthquake warrant clarification. First, even though there are three separate depth ranges bounded by the 75% contour, the initiation depths of the deeper two are separated by less than 15 km. Therefore, based upon the definitions given above, this earthquake is classified as having only two rupture planes (Table 2). Second, there is low amplitude energy that is visible at about 25 s after the hypocentral time at a depth of 50 km. This is an artifact that arises for shallow events due to the *pP* phase arrival within the *P* wave window used in the back projection analysis. If the back projection method is applied to events shallower than 100 km, the amplitude of this artifact can become quite large at times close to the hypocentral time, complicating source imaging and degrading the depth resolution.

5.3. Hindu Kush

[24] The intermediate-depth seismicity in Hindu Kush and Pamir is thought to be taking place within a remnant slab that was subducting beneath Eurasia during its collision with India around 55 Ma [e.g., *Pavlis and Das*, 2000]. A total of 4 earthquakes with magnitudes between 6.5 and 7.4 are studied from this region with depths between 187 and 230 km (Figure 10 and Table 3). Three of these events have simple ruptures (Figures 10b, 10c, and 10d). For all three events, bivertical (upward and downward) energy propagation is observed. The durations range from 13 to 15 s, and the vertical extents range from 15 to 30 km. Some of the subevents in this region have symmetric depth behavior (Figures 10b and 10d) that is similar to that observed for synthetic results (section 4). As was discussed in the previous section, these symmetric low amplitude stacks may be artifacts, and therefore, part of the complexity seen may not reflect the actual rupture properties of the subevents. The fourth and largest event of this group of earthquakes (Mw 7.4) is composite and characterized by three subevents. The two strongest subevents which dominate the earthquake are separated by 75 km (Figure 10a). The total duration of this event is 21 s.

Figure 9. Same as Figure 8 but for events in Vanuatu. The slab contours are from 50 to 400 km. See Table 2 for a summary of the results. (a) The 8 September 2008 event with magnitude Mw 6.9 at a depth of 110 km. (b) The 8 February 2005 event with magnitude Mw 6.7 at a depth of 206 km. (c) The 9 January 2001 event with magnitude Mw 7.1 at a depth of 103 km. (d) The 7 August 2006 event with magnitude Mw 6.8 at a depth of 149 km. (e) The 9 April 2004 event with magnitude Mw 6.5 at a depth of 228 km. (f) The 4 March 2010 event with magnitude Mw 6.5 at a depth of 176 km. (g) The 1 August 2007 event with magnitude Mw 7.2 at a depth of 120 km. (h) The 6 November 2003 event with magnitude Mw 6.6 at a depth of 113 km.

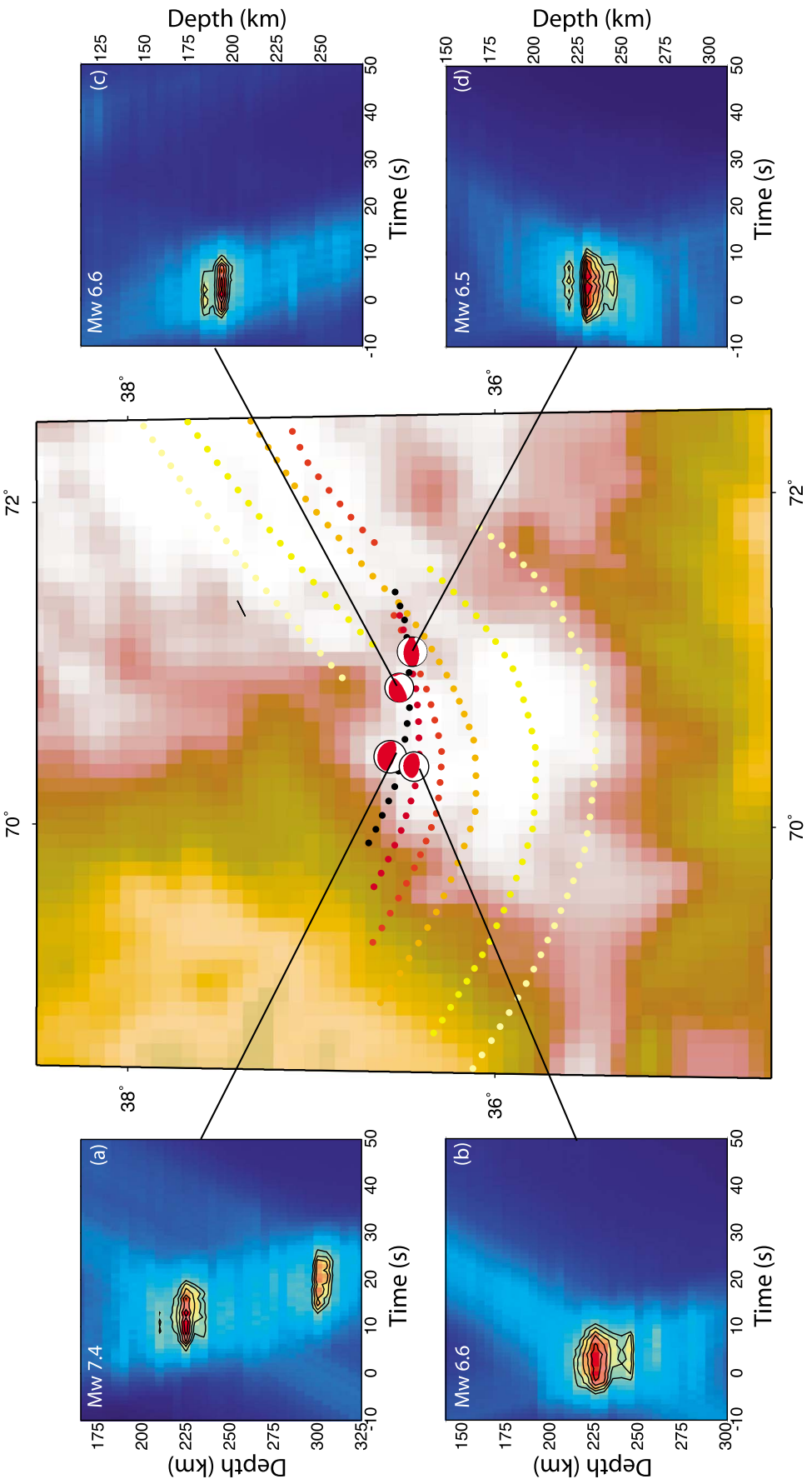

Figure 10. Same as Figure 8 but for events in Hindu Kush. The slab contours are from 50 to 300 km. See Table 3 for a summary of the results. (a) The 3 March 2002 event with magnitude Mw 7.4 at a depth of 225 km. (b) The 3 January 2009 event with magnitude Mw 6.6 at a depth of 204 km. (c) The 5 April 2004 event with magnitude Mw 6.6 at a depth of 187 km. (d) The 12 December 2005 event with magnitude Mw 6.5 at a depth of 230 km.

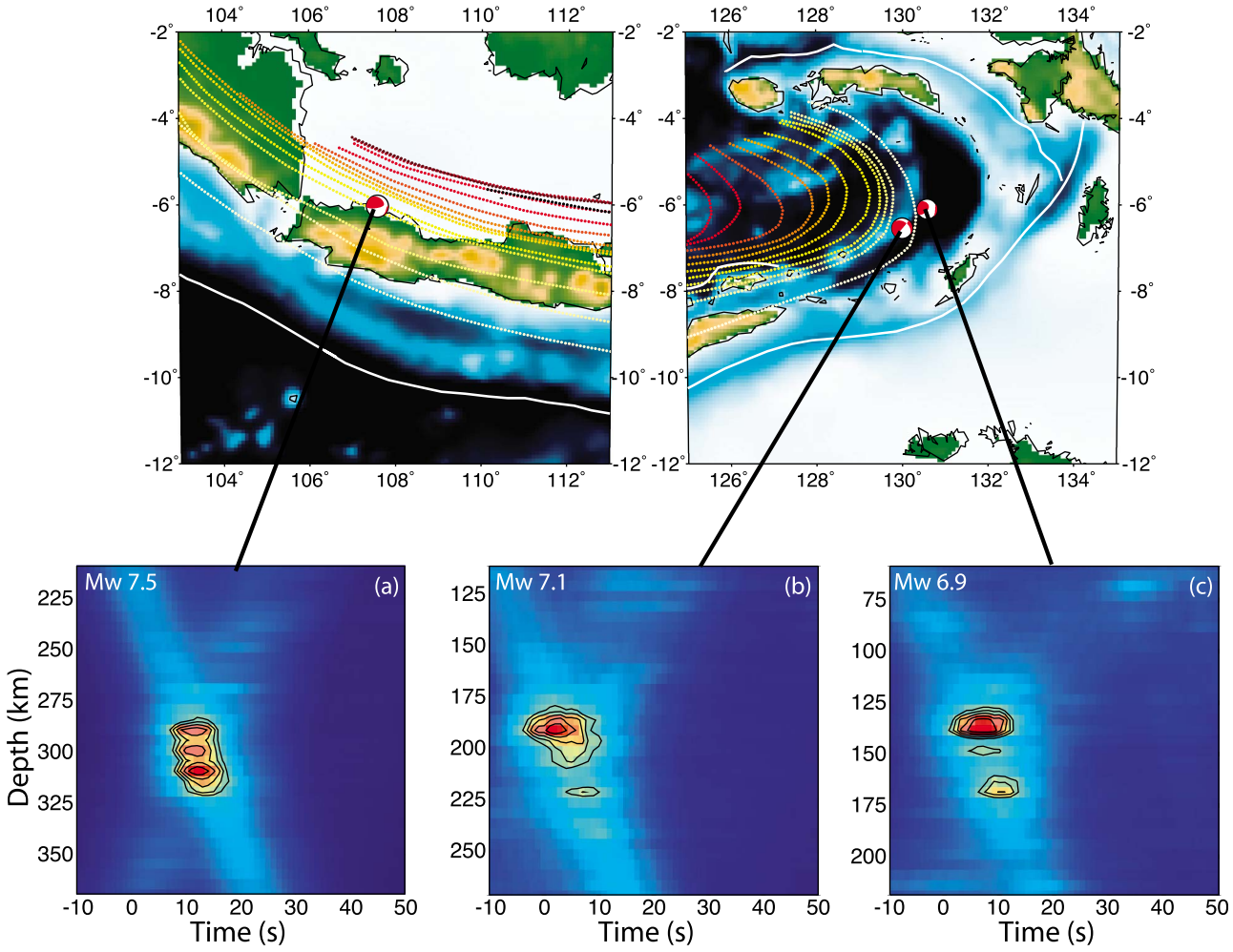

Figure 11. Same as Figure 8 but for events in Java. The slab contours are from 50 to 700 km. See Table 4 for a summary of the results. (a) The 8 August 2007 event with magnitude Mw 7.5 at a depth of 280 km. (b) The 2 March 2005 event with magnitude Mw 7.1 at a depth of 191 km. (c) The 24 October 2009 event with magnitude Mw 6.9 at a depth of 138 km.

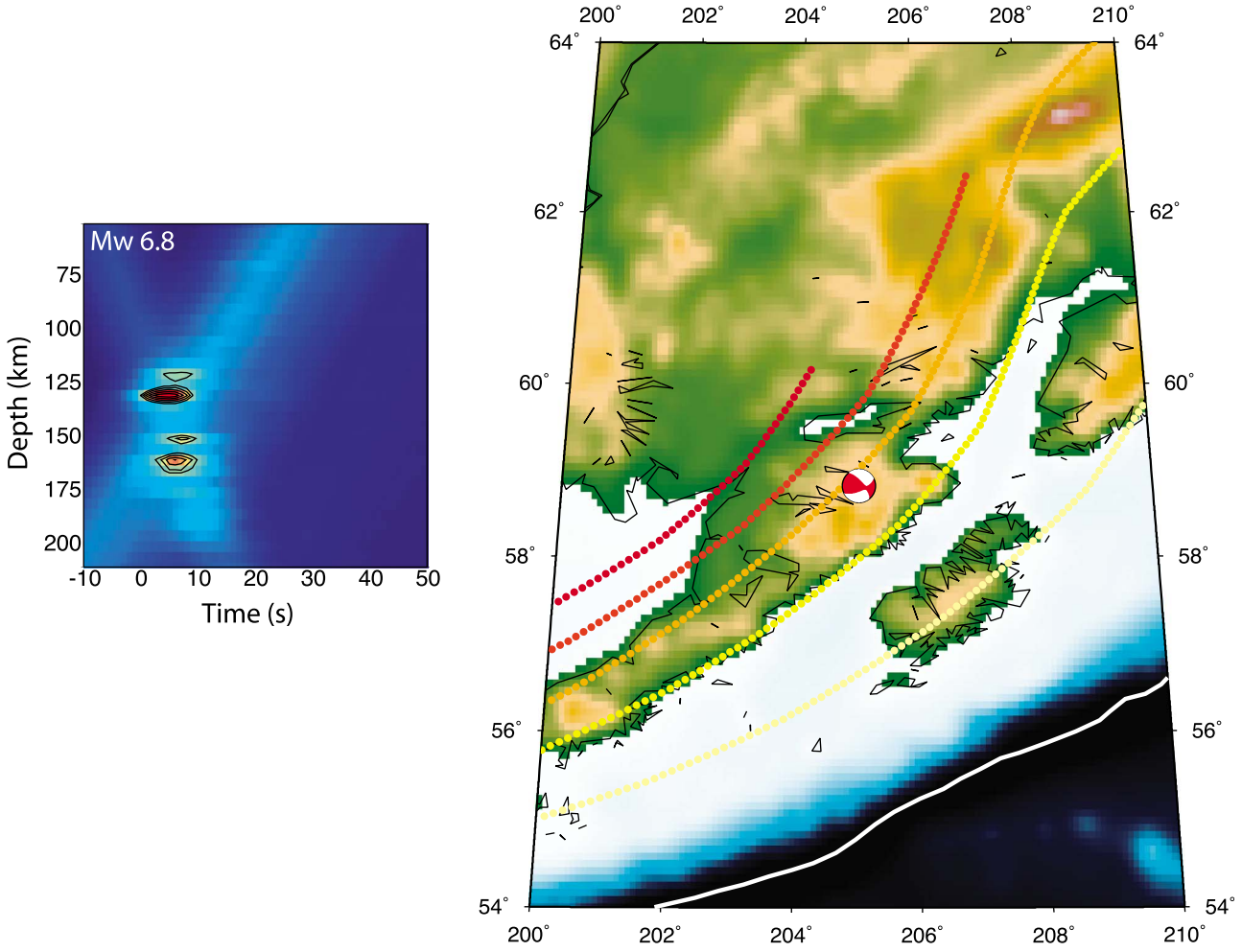

Figure 12. Same as Figure 8 but for the event in Alaska. This earthquake occurred on 28 July 2001, had a magnitude Mw 6.8, and a hypocentral depth of 131 km. The slab contours are from 50 to 250 km. See Table 5 for a summary of the results.

5.4. Java

[25] Along the Java trench, the Indo-Australian plate subducts beneath the Eurasian plate. The age of the Indo-Australian plate at the subduction zone varies from 50 Myr in the east to 140 Myr in the west [*Holcombe*, 1977]. All three of the earthquakes from this region have relatively large magnitudes (Mw $\geq$ 6.9). The main ruptures of all of these events also have large vertical extents (20–35 km) with mainly downward propagation (Table 4 and Figure 11). For two of these earthquakes, there are subevents separated by 15 km or more and therefore they are composite earthquakes (Figures 11b and 11c). The event durations of the Java earthquakes range from 9 to 13 s.

5.5. Alaska

[26] In this region, the Pacific plate subducts beneath the North American plate along the Aleutian trench at a rate of 7 to 8 cm/yr, and unlike most sections of the Aleutian trench, convergence is perpendicular to the trench [*Creager and Boyd*, 1991]. The one earthquake studied in this region has a large strike-slip component based upon the Global CMT solution, and is observed to be a composite rupture (Figure 12). The first rupture propagates 10 km upward, although the energy falls below the 75% level during this upward propagation. The second rupture starts 30 km below the initial rupture and propagates both upward and downward, and has a total vertical extent of 15 km. The event duration of this earthquake is 9 s.

6. Discussion

[27] The depth-time behavior of these intermediate-depth events can be interpreted in many different ways. However, we first address the issue of whether the complexities of the composite ruptures are artifacts of the back projection method or effects due to seismic phases that are not included in the analysis. In order to investigate the robustness of the complexities imaged by the back projection technique, additional synthetic tests are presented in this section with a focus on the large Hindu Kush event which had the largest depth separation between two rupture planes. These tests support the conclusion that multiple planes of high amplitude energy are real features of the earthquakes.

6.1. Robustness of Composite Ruptures

[28] The composite earthquakes are potentially the most interesting observations of this study (e.g., Figure 10a). These results are partially supported by reports of similar complexity in other catalogues for some of the events we have analyzed [e.g., *Starovoit et al.*, 2002]. We investigate whether complexities seen in the back projection results are real features of the events or artifacts of the stacking procedure. As the synthetic results show, high amplitude artifacts do not arise when the input source is simple (Figures 6 and S2). However, this may not necessarily apply to very complex ruptures. To investigate this possibility, a more complex case is simulated by using the *P* wave train recorded at a single station from the 3 March 2002 Hindu Kush event (Figure 10a) as the input source time function for a synthetic test (Figure 13a). The hypocentral location of this complex synthetic source is fixed to that of the Hindu Kush event, i.e., 36.50°N latitude, 70.48°E longitude, and 225 km depth. If the second rupture observed in the 3 March 2002 Hindu Kush event is an artifact of the complex source time function, then a similar artifact should be seen in the synthetic result. On the other hand, if the method can reliably constrain depth for the complex source time function, then the synthetic result should have high amplitude stacks only at the assigned depth. Figure 13b shows the high amplitude energy is imaged at the hypocentral depth, although there is low amplitude energy above and below the assigned depth of 225 km. This result demonstrates that even for a very complex horizontal rupture, artifacts of high amplitude energy at different depths are suppressed by virtue of using multiple seismic phases.

[29] There is also the possibility that seismic phases not included in the back projection analysis may cause the observed complexity. As demonstrated in an earlier section (Figure 6) and discussed briefly for an event in the Vanuatu region (Figure 9h), moderately coherent stacks can result at depths and times close to the hypocenter when unwanted phases are present. To investigate this possibility, we focus on crustal and water phases, which have very similar raypaths as the depth phases used in this study. In particular, we consider arrivals due to underside reflections from the Moho and the sea surface. To determine the effect of these phases on back projection results, the synthetic tests used in Figure 6 are modified. For the original synthetic tests, seismograms include one Ricker wavelet for each assigned point source and each seismic phase chosen for that source, i.e., one Ricker wavelet for each of the *P*, *pP*, and *sP* arrivals. This approach is changed so that more Ricker wavelets arrive around the depth phase time to mimic the crustal and water reflection phases while the *P* arrival consists of a single Ricker wavelet.

[30] We determine the time shifts for the phases that interact with the crust and ocean using a 7 km thick crust, a 3 km thick ocean, and velocities from the one-dimensional model IASP91 [*Kennett and Engdahl*, 1991]. For the underside reflection at the Moho, a Ricker wavelet is assigned to arrive before both depth phases (*pP* and *sP*). For the *pP* phase, the time shift of −2.4 s is calculated using the two-way travel time of a *P* wave through the crust. For the *sP* phase, the time shift of −3.3 s is calculated by summing the one-way travel times of *P* and *S* waves in the crust. For both calculations, we make the approximation that the raypaths within the crust are vertical. To estimate the arrival times of the water phases, we use the two-way travel time of a *P* wave in the ocean. Once again, a vertical path is assumed, and the time shift is 4.1 s with respect to the *pP* and *sP* arrival time. Figures 14b and 14c show that there is little change in the imaged energy of the depth phases for these synthetic tests compared to a single point source (Figures 6b and 6c) although there is a slight extension in time. This is because the additional phases associated with the crust and ocean have origin times that are within or very close to the temporal uncertainty of the single point source (±5 s). The combined result shows that the additional arrivals do not cause high amplitude artifacts at different depths, and produce results almost identical to a point source. This approach assumes that phases associated with the crust and ocean can be represented by time shifted depth phases and ignores deviations in the slowness from the depth phases. These deviations in slowness are small, but if they were included when generating the synthetic seismograms, it would only decrease the stack amplitudes due to the fact that a different slowness would reduce coherent stacking of the additional phases using *pP* or *sP* arrival times. Therefore, the synthetic test shown in Figure 14 gives the maximum effect that can be produced by these phases.

[31] We have only considered underside reflections in these synthetic tests and ignored multiple reflections within the crust and water column. Each reflection will change the slowness of these phases further away from that of the slowness of the depth phases used in the back projection analysis. Therefore the stack amplitudes should be smaller than the underside reflections and contribute less to any possible artifacts. An additional source of complexity may be the seismic wave interactions with the subducting slab. We assume that any phases produced by these interactions would have lower amplitudes compared to the *P* and depth phases, however, only by fully modeling the wavefield with three-dimensional structure can we confirm this assumption, and, therefore, slab interactions are a potential source of error. On the other hand, arrivals such as slab reflected phases would produce stacks with the same time dependence for various "subevents" which is not observed for most of the composite earthquakes. Therefore we believe that the artifacts due to the presence of a slab are not significant in most of our results.

6.2. Properties of Composite Ruptures

[32] Based upon various resolution tests, the imaged energy of the composite earthquakes is a real feature of rupture complexity. We explore this complexity further in this section. First, the timing of the individual subevents for some of the composite events are such that dynamic triggering by seismic waves is likely to be involved in the activation of the second subevent. For example, the 3 March 2002 Hindu Kush event shows a depth separation of 75 ± 5 km between individual subevents. The time separation between the initiation of the two subevents is about 8.5 ± 2.0 s, which implies that the minimum speed required to relate the two subevents is around 9 ± 2 km/s (Figure 15). This velocity is in the range of compressional wave velocities, including those within the slab imaged from tomographic studies in the Hindu Kush region [e.g., *Koulakov and Sobolev*, 2006], but is too high for shear waves, which at 200 km depth have velocities around 4.5 km/s [*Kennett and Engdahl*, 1991]. The potential mechanism by which a compressional wave from one rupture

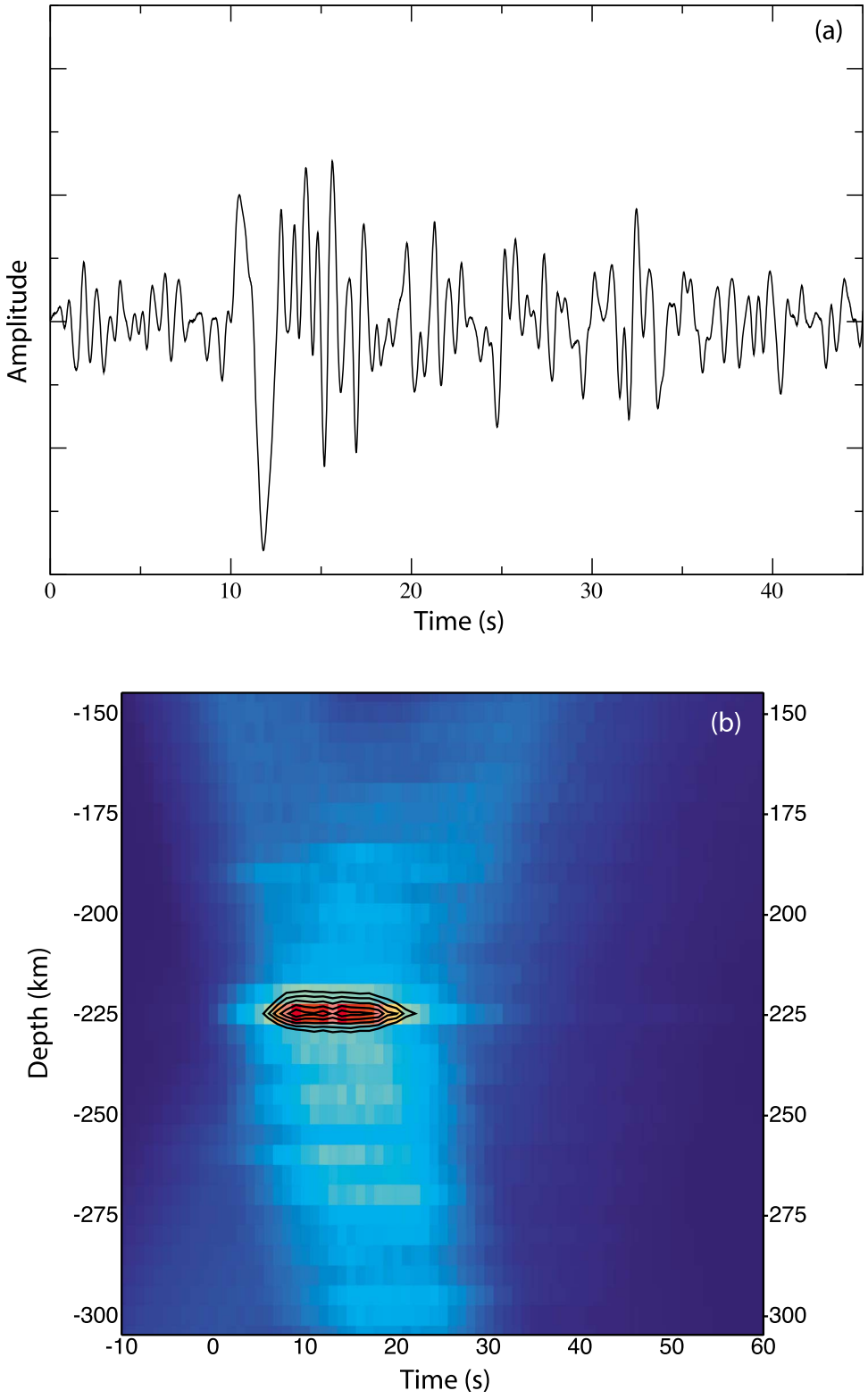

Figure 13. Synthetic test with a complex source time function. (a) Instead of using a simple Ricker wavelet (Figure 4a), this synthetic test uses the *P* waveform from the 3 March 2002 Hindu Kush recorded at station MIGH as the source time function. (b) Back projection result where the input source is located at 36.50°N, 70.48°E, and 225 km depth, i.e., a point source. For this synthetic test, only the *P* and *sP* seismic phases are used in the back projection analysis since these are the phases used for the actual earthquake.

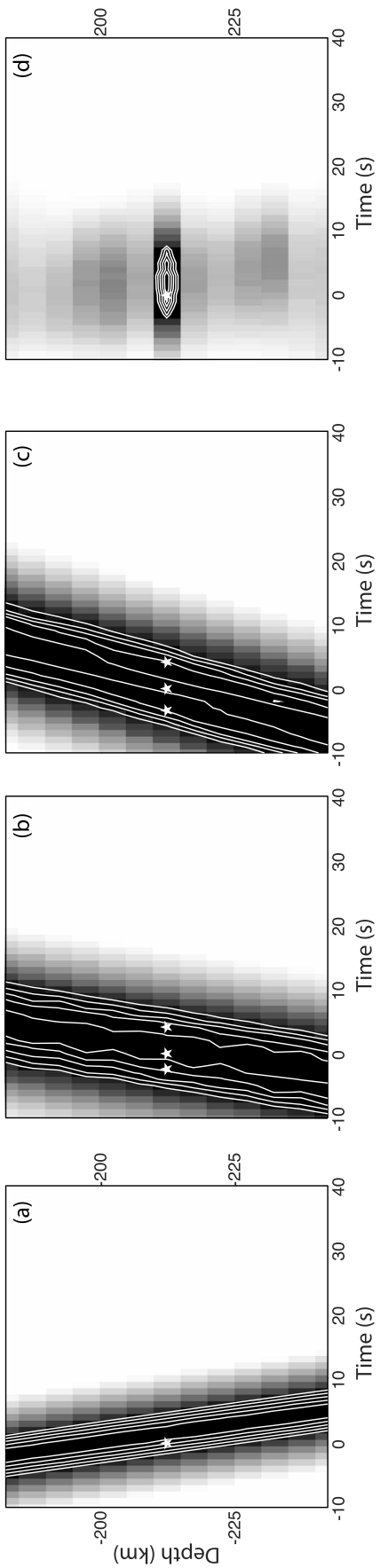

Figure 14. Effects of the crust and water layers. The back projection result from a point source using only the *P* phase, as well as the back projection result from the depth phases with additional sources included to simulate phases produced by bottom side reflections of the crust and the water surface. (a) The back projection result from a single point source (black star) using only the *P* phase. (b) The back projection result from three point sources (black stars) with the same hypocentral locations, but different origin times using *pP* travel times. The first star mimics the underside reflection at the Moho that arrives 2.4 s before the *pP* phase. This time is calculated using a 7 km thick crust with a *P* wave velocity of 5.8 km/s from IASP91 [*Kennett and Engdahl*, 1991]. The second star is the hypocenter generating the *P* wave arrival. The third star mimics the underside reflection at the ocean surface that arrives 4.1 s after the *pP* phase. This time is calculated using a 3 km thick ocean with a *P* wave velocity of 1.45 km/s from IASP91 [*Kennett and Engdahl*, 1991]. (c) The back projection result from three point sources (black stars) with the same hypocentral locations, but different origin times using *sP* travel times. The first star mimics the underside reflection at the Moho that arrives 3.4 s before the *sP* phase. This time is calculated using a 7 km thick crust with *P* and *S* wave velocities of 5.8 km/s and 3.36 km/s from IASP91, respectively [*Kennett and Engdahl*, 1991]. The second star is the hypocenter generating the *P* wave arrival. The third star mimics the underside reflection at the ocean surface that arrives 4.1 s after the *sP* phase. This time is calculated using a 3 km thick ocean with a *P* wave velocity of 1.45 km/s from IASP91 [*Kennett and Engdahl*, 1991]. (d) The back projection result using all three seismic phases with the simulated bottom side reflections included.

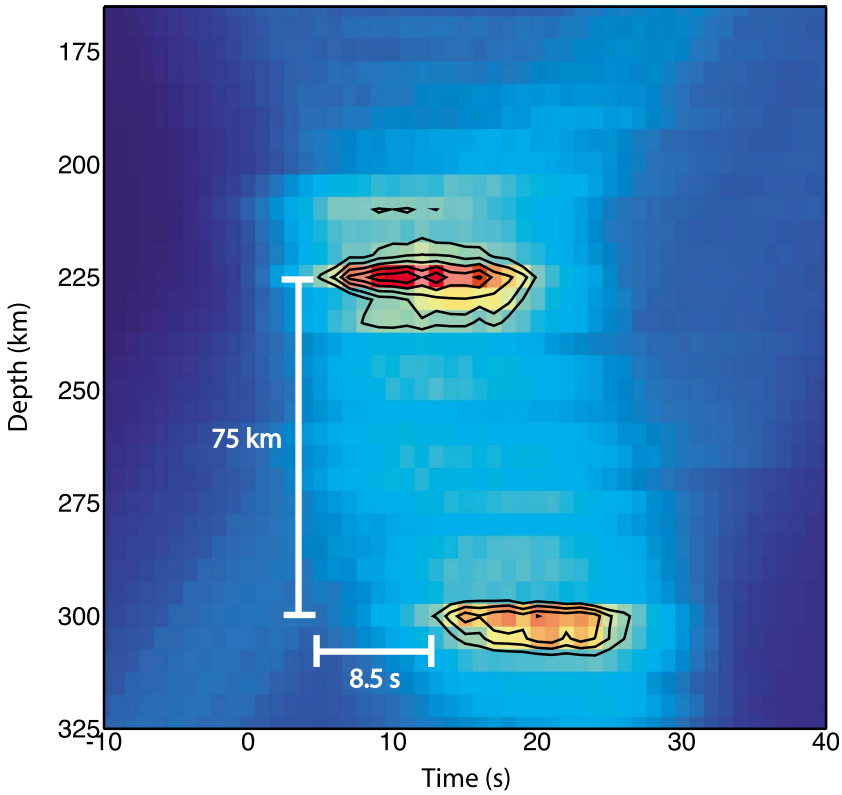

Figure 15. Dynamic triggering. The back projection results from the 3 March 2002 Mw 7.4 Hindu Kush event. The two ruptures of this event are separated by 75 km in depth and 8.5 s in time. This leads to a propagation velocity of 8.8 km/s, which is close to the *P* wave velocity in this region.

would trigger a second rupture is discussed in a subsequent section. Another characteristic of the composite events is that often the individual subevents have very different depth-time behavior. For example, the 9 December 2007, Mw 7.8 event has two ruptures which have considerable time overlap (Figure 8b). While the bottom rupture propagates upward with time, the top rupture maintains the same depth throughout its duration. This behavior suggests that the two ruptures are independent of one another.

[33] The existence of multiple subevents involving two independent faults can have effects on the non-double-couple components of the moment tensors [e.g., *Houston*, 1993]. These components are quantified using the parameter ϵ defined as $\epsilon = -\lambda_2/\max(\lambda_1, \lambda_3)$ where λ values are the eigenvalues of the moment tensor with $\lambda_1 \geq \lambda_2 \geq \lambda_3$ [e.g., *Ekström*, 1994]. This parameter varies from 0.0 for a double-couple source to ±0.5 for a purely non-double-couple source (i.e., compensated linear vector dipole). Using the Global CMT catalogue, the average absolute epsilon value of the events classified as "composite" in this study is 0.16, over twice that of the "simple" events (0.07). Furthermore, all five events with absolute epsilon values above 0.15 are imaged by the back projection method as composite events. These results support the interpretation that subevents are occurring as separate rupture planes.

[34] Another property which may be related to the existence of composite events is the earthquake magnitude. Composite ruptures characterize most of the largest events studied, although there are a few smaller events (Mw < 7.0) which exhibit this behavior (e.g., Figure 9h). This observation suggests that the largest intermediate-depth earthquakes involve multiple faults. This interpretation also suggests that there could be predetermined rupture dimensions for any given region, which may be defined by preexisting faults in the slab. One test for this hypothesis is to determine the magnitude at which composite ruptures occur for different subduction zones or even different sections of the same subduction zone, though more than 22 events are needed to obtain statistically significant conclusions.

[35] In addition, earthquake magnitude has been shown to be related to the duration of the event for shallow earthquakes in a relationship expected from a circular rupture model, i.e., $\tau \propto M_o^{1/3}$, where τ is the event duration and M_o is seismic moment [e.g., *Vidale and Houston*, 1993]. Multiple studies have investigated this relationship for intermediate-depth earthquakes [e.g., *Vidale and Houston*, 1993; *Bos et al.*, 1998; *Houston et al.*, 1998; *Campus and Das*, 2000; *Houston*, 2001; *Persh and Houston*, 2004], and these studies have found that the durations of the largest intermediate-depth events tend to be shorter than expected from the magnitude-duration relationship observed for shallow earthquakes. The results presented in this manuscript offer a possible explanation for this behavior. If two faults are rupturing at the same time, the duration recorded on seismograms should be much shorter than the duration of an event on a single fault with the same magnitude. As Tables 1–5 show, summing the durations of individual subevents leads to longer cumulative durations than the event durations discussed earlier. These observations

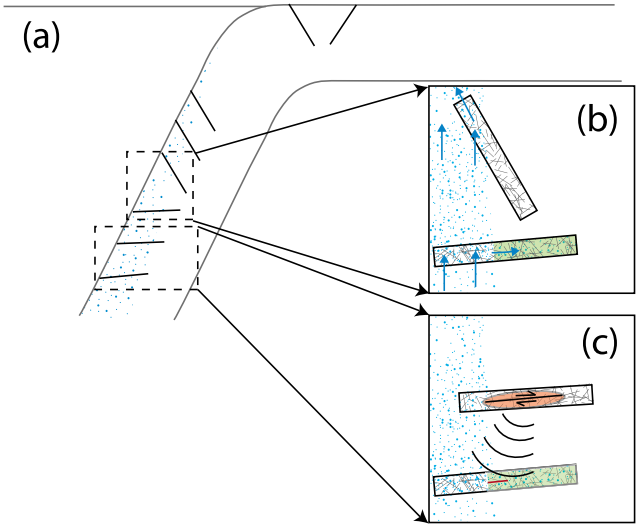

Figure 16. Proposed mechanism. Cartoon of a slab subducting into the mantle with preexisting fault fabric and the mechanisms responsible for the generation and triggering of intermediate-depth earthquakes. (a) Schematic of the orientation of the preexisting faults (black lines) when they develop at the outer rise and after plate subduction. The blue stippled region depicts dehydration of the slab as it subducts into the mantle. (b) Enlarged view of the two conjugate faults (damage zones within the fault depicted by cross hatching) at intermediate depth. The blue arrows show propagation of water as it dehydrates from the slab and travels into the mantle wedge. Water would propagate deep into the slab more efficiently along a subhorizontal fault with near constant pressure as opposed to a steeply dipping fault for which the grain size difference may not be strong enough to effectively oppose the pressure gradient. The green region depicts the hydrated material. (c) Detailed schematic of the processes around preexisting faults. Rupture on one subhorizontal fault (red region with opposing arrows) generates seismic waves (curved black lines) that trigger slip (red line) on a second fault that has been weakened by water focusing and serpentinization. This initial slip will generate heat which will dehydrate the surrounding serpentine and lead to the positive feedback between dehydration embrittlement, slip, and heat generation discussed in the main text.

may explain why the largest intermediate-depth earthquakes have shorter durations than expected, however, more data are needed to test this hypothesis.

6.3. Depth Variation of Individual Subevents

[36] In this section, we explore the implications of the subevent vertical extents in terms of fault geometry, slip, and rupture propagation. The frequent observation of subevents with limited depth extent is consistent with recent directivity studies that found a predominance of subhorizontal rupture planes for large, intermediate-depth earthquakes [*Warren et al.*, 2007, 2008]. Other studies have also observed this behavior for a small number of events [e.g., *Suzuki and Kasahara*, 1996; *Antolik et al.*, 1999; *Tibi et al.*, 2002; *Delouis and Legrand*, 2007]. However, the back projection method cannot distinguish subhorizontal rupture propagation from a stationary source, i.e., energy release from the same point location over a period of time. This scenario is unlikely for most of the subevents considered in this study in which the duration is significantly longer than the time uncertainty of ±5 s, and based upon the magnitude, slip is expected to occur over a relatively large area. Another shortcoming of the back projection technique is uncertainty in the slip direction. Thus, given the typical focal mechanisms of the earthquakes studied, the depth-limited subevents can be interpreted as having slip vectors that are parallel to the propagation direction (i.e., slip on a subhorizontal plane) or having vertical slip (i.e., slip perpendicular to the propagation direction). In the latter case of vertical slip, the fault will require an uncommon aspect ratio compared to typical slip observed at shallow depths, i.e., a very thin (depth dimension) and long (lateral dimension) fault. Regardless of the slip direction, our observations require significant lateral and limited depth extents of the fault, and following previous studies [e.g., *Warren et al.*, 2007, 2008], we interpret the subevents to have subhorizontal rupture planes.

7. The Mechanism of Intermediate-Depth Earthquakes

[37] The observations presented in this study show that most of the large, intermediate-depth earthquakes have small vertical extents of energy release, which we interpret as slip on shallowly dipping rupture planes. We also find that a significant number of these events have multiple rupture planes that are clearly separated in depth. These constraints provide insight into the possible mechanism of large, intermediate-depth events. In this section, we briefly review possible fault orientation scenarios, followed by a comparison of our findings with previously proposed mechanisms, and provide a new hypothesis for the generation of large intermediate-depth earthquakes.

7.1. Orientation of Possible Faults

[38] The observation of shallowly dipping rupture planes suggests that either an isobaric process is generating large, intermediate-depth earthquakes, or there are weak zones within the subducting slab that all have a subhorizontal orientation [*Warren et al.*, 2007, 2008]. For the latter case, one candidate for weak zones is faults generated at the outer rise [e.g., *Savage*, 1969; *Jiao et al.*, 2000; *Ranero et al.*, 2005]. Multiple studies using a variety of methods, such as seabeam mapping, seismic reflection, and aftershock distributions, have imaged the orientation of outer-rise faults [e.g., *Masson*, 1991; *Kobayashi et al.*, 1998; *Ranero et al.*, 2003, 2005; *Fromm et al.*, 2006; *Hino et al.*, 2009]. These studies show that the outer-rise faults, associated generally with bending and subduction of the plate, strike subparallel to the trench. With the possible exception of Central America [e.g., *Ranero et al.*, 2003], they also show the formation of grabens with conjugate faults dipping toward and away from the trench [e.g., *Masson*, 1991; *Kobayashi et al.*, 1998; *Ranero et al.*, 2005; *Fromm et al.*, 2006; *Hino et al.*, 2009] and dip angles typically between 30 and 60 degrees [e.g., *Savage*, 1969; *Jiao et al.*, 2000]. During subduction, these faults are rotated by the dip angle of the subducting slab which is typically between 40 and 60 degrees [e.g., *Luyendyk*, 1970; *Cruciani et al.*, 2005], resulting in a set of faults that are nearly horizontal and vertical at depth (Figure 16a) [e.g., *Savage*, 1969;

Jiao et al., 2000]. If these features are associated with intermediate-depth earthquakes, then an explanation must be provided for the preferential reactivation of subhorizontal faults at depth.

[39] Subhorizontal rupture planes may also suggest the importance of isobaric processes in generating large, intermediate-depth earthquakes. One possibility is that transformational faulting is generated through a phase change as minerals are subducted to higher pressures. The main problem with this hypothesis is that the minerals which undergo phase transformations at intermediate depths only make up a small percentage of the subducting slab, and therefore could not generate a large rupture [*Green and Houston*, 1995]. Alternatively, it is possible that fluids, which facilitate rupture, follow an isobaric path under certain conditions. We will revisit this fluid path argument in a later section.

7.2. Previously Proposed Mechanisms

[40] Unlike shallow earthquakes, high pressures at intermediate depths should prohibit crack formation and brittle failure due to simple strain accumulation. Hypotheses for the mechanism of intermediate-depth earthquakes are therefore much different than those of shallow events and include partial melting [e.g., *Savage*, 1969], transformational faulting [e.g., *Green and Burnley*, 1989], localized shear instabilities [e.g., *Ogawa*, 1987; *Hobbs and Ord*, 1988], localized viscous creep due to a grain size difference within and outside the faults [*Keleman and Hirth*, 2007], and dehydration embrittlement [e.g., *Raleigh and Paterson*, 1965; *Kirby et al.*, 1996; *Hacker et al.*, 2003; *Jung et al.*, 2004]. As will be explained below, both localized viscous creep and dehydration embrittlement are promoted by the presence of preexisting faults. Based upon the observation of preferential subhorizontal rupture plane orientations, we assume that intermediate-depth earthquakes are associated with preexisting zones of weakness. Therefore, we will focus on localized viscous creep and dehydration embrittlement as possible mechanisms.

7.2.1. Localized Viscous Creep

[41] Recent modeling work [i.e., *Keleman and Hirth*, 2007] has shown that shear heating due to localized viscous creep along fine-grained shear zones can produce instabilities and potentially generate earthquakes within the temperature range (600 to 800°C) commonly associated with intermediate-depth events [*Peacock*, 2001]. If these fine-grained zones within preexisting faults are the conjugate faults developed at the outer rise, it would be expected that this localized viscous creep mechanism would operate on both the subvertical and subhorizontal faults. This is contrary to the observation that most large intermediate-depth earthquakes have subhorizontal rupture planes [*Suzuki and Kasahara*, 1996; *Delouis and Legrand*, 2007; *Warren et al.*, 2007, 2008]. However, it may be possible to prevent reactivation of vertical faults at intermediate depths if conditions for vertical and horizontal faults differ. For the localized viscous creep mechanism, the temperature and grain size difference of the fault are the controlling parameters. If the temperature becomes too high, above 850°C [*Keleman and Hirth*, 2007], displacement will be accommodated by steady state flow instead of instabilities. It has been observed that trenchward dipping faults (subvertical faults at intermediate depths) are preferentially activated close to the trench [e.g., *Masson*, 1991]. This behavior is caused by the shear stresses imparted as the slab subducts beneath the overriding plate, which is likely to continue until the slab becomes coupled to the surrounding mantle. It is possible that preferential activation of these faults would cause an increase in their temperature and thus limit their rupture at intermediate depths. This explanation, however, is unsatisfactory because heating due to rupture on vertical faults may also affect the temperature of the material surrounding the subhorizontal faults. In addition, the preferential slip on the trenchward dipping faults would also lead to smaller grain sizes for the nearly vertical faults compared to subhorizontal faults. This difference in the grain sizes within the fault gouge would promote slip on vertical faults based upon the localized creep mechanism. Therefore, localized viscous creep alone can not explain the observed tendency of rupture on subhorizontal planes.

7.2.2. Dehydration Embrittlement

[42] Another proposed mechanism that has become popular over the past twenty years is dehydration embrittlement [e.g., *Raleigh and Paterson*, 1965; *Kirby et al.*, 1996; *Hacker et al.*, 2003; *Jung et al.*, 2004]. This mechanism argues that when water is released from hydrous minerals at depth, it increases the local pore pressure enough to counteract the confining pressure, allowing brittle failure. In order to account for the required existence of hydrous minerals, this mechanism is often described in association with faults that develop at the outer rise where water can propagate deep into the mantle and hydrate the fault. This fault hydration at the surface would not create a significant difference in the amount of hydration between the faults that dip toward (vertical at intermediate depths) and away from (horizontal at intermediate depths) the trench. If anything, the preferential activation of the trenchward dipping faults would allow more vertical faults to be hydrated. Therefore, without considering additional mechanisms, dehydration embrittlement of the outer-rise faults hydrated at the surface can not explain the predominance of subhorizontal ruptures. Another potential problem is that the hydrous minerals must be preserved from the surface to great depths over many earthquake cycles. Finally, the stress changes from compressional waves should have a similar influence on the pore pressures of subhorizontal and vertical faults, and therefore dehydration embrittlement alone can not explain the observed preferentially triggered subhorizontal ruptures. *Kuge et al.* [2010] studied an earthquake in Tarapaca, northern Chile that occurred at a depth of 110 km, and observed two subevents separated in depth, a result similar to those presented in this manuscript. They propose that these subevents represent the results of dehydration embrittlement in the upper crust and mantle [e.g., *Peacock*, 2001] during rupture of a fault that cuts through both, i.e., the subevents correspond to the top and bottom seismicity of double Wadiati-Benioff zones. This mechanism may be able to explain some of the back projection observations at the shallowest depths considered here. However, many of the earthquakes we study take place deeper than the depths at which double seismic zones are observed.

7.3. Proposed Mechanism for Intermediate-Depth Earthquakes

[43] The discussion above demonstrates that the available mechanisms for the occurrence of intermediate-depth

earthquakes can not satisfy the observations of preferential activation of subhorizontal rupture planes and *P* wave triggering of subevents. In this section, we propose a new mechanism for the generation of these earthquakes.

7.3.1. Subhorizontal Rupture Planes

[44] The preference of subhorizontal rupture planes at intermediate depths can be explained by considering post-subduction dehydration and preexisting fault fabric. At the depths relevant to this study, i.e., between 100 and 300 km, the slab releases water as it reaches higher temperatures and pressures, and the water migrates toward the mantle wedge (Figure 16a). Some of this water will encounter the preexisting faults along its migration path. The faults are characterized by smaller grain sizes compared to the surrounding material, and the difference in the grain sizes acts to concentrate water under these temperature and pressure conditions [*Wark and Watson*, 2000]. The water trapped in the faults can migrate along the fine-grained material, and once it reaches the interior of the slab where hydrous minerals are stable, the faults can be replenished with hydrous minerals [e.g., *Schmidt and Poli*, 1998]. This water migration into the slab would be more efficient along the subhorizontal faults since the pressure is nearly constant along these faults and the grain size difference inhibits further vertical migration (Figure 16b). In contrast, water intersecting the vertical faults near the top surface of the slab experiences the same grain size effect that tries to focus water within the fault zone, but downward migration into the serpentine stability zone within the slab must happen against the pressure gradient and buoyancy. This opposing force would likely limit the amount of water penetration into the slab interior and hence the rate at which subvertical faults can be replenished with hydrous minerals.

[45] This difference in the rate at which hydration of subvertical and subhorizontal faults can take place makes many more weaker subhorizontal faults, allowing shear localization and instability to occur [e.g., *Keleman and Hirth*, 2007]. Once shear failure initiates, a temperature increase due to frictional heating and strain hardening [*Chernak and Hirth*, 2010] will dehydrate the hydrous minerals [e.g., *Schmidt and Poli*, 1998] to enhance the condition for slip. This constitutes a positive feedback mechanism where the temperature increase due to slip on one part of the fault causes dehydration of hydrous minerals on adjacent parts of the fault, promoting further slip. It is also possible that each rupture event will extend the damage zone into deeper and colder parts of the slab. The finer-grained material of these new damage zones will concentrate water and generate hydrous minerals, allowing replenishment and reactivation of preexisting faults to greater depths.

[46] There are a few points of this hypothesis which are worth reemphasizing. First, the mechanism described above does not necessarily apply to smaller events. The initiation of rupture due to the small grain size of the fault zone may be enough to produce small ruptures on faults of any orientation. However, the runaway dehydration reaction will better accommodate the large rupture areas required for large earthquakes. Second, it has been suggested that fault zones would grow into the slab with each rupture. This growth would allow parts of the fault zones to remain within the cold slab, allowing for mineral hydration, even as this region becomes smaller as the slab warms. Finally, many studies have argued that outer rise faults are hydrated well into the mantle before subduction, and this hydration is what allows faults to be reactivated as depicted by double seismicity zones [e.g., *Peacock*, 2001; *Ivandic et al.*, 2010]. The hypothesis proposed in this study does not preclude hydration at the surface, but puts more emphasis on hydration within the slab after subduction for generating large, intermediate-depth earthquakes. The faults are expected to lose water when an earthquake occurs, so the replenishment will also help explain the great depths to which earthquakes are observed.

7.3.2. Dynamic Triggering

[47] The hypothesis for the preferential occurrence of rupture on subhorizontal planes must also be consistent with the observation that dynamically triggered multiple ruptures commonly contribute to a large event. Theoretical work at low temperatures and pressures relevant for shallow-focus earthquakes has shown that for faults with significantly lower shear moduli, the pore pressures, and hence effective normal stress, are controlled by fault-normal stresses [*Cocco and Rice*, 2002]. Extending this argument to faults at depth, the interaction of the compressional wave, therefore, could reduce the effective normal stress on a hydrated fault through elevated pore pressure. If shear has already been localized on the fault through mechanisms such as viscous creep localization, the sudden reduction in effective normal stress will initiate slip. Our observations show that the triggered rupture planes are also subhorizontal, and therefore, these faults may contain a sufficient amount of hydrous minerals to experience the same positive feedback process proposed to explain the preferential slip on subhorizontal faults.

[48] Given the runaway dehydration mechanism, at least two conditions must be satisfied for two faults to ultimately rupture together. First, the stress state of the two faults must be very similar. Even with stress perturbations from seismic waves, the shear instability that initiates both ruptures requires hundreds of years of stress buildup before it becomes feasible [*Keleman and Hirth*, 2007]. Recent work on shallow earthquakes may be able to explain this fault synchrony. If two nearby faults have similar dimensions, orientations, and slip rates, then the static stress changes from rupture on each fault may, over the course of many earthquake cycles, bring the rupture cycles of the two faults into phase. When this occurs, the two faults will become locked in phase [*Scholz*, 2010]. It seems possible that this same mechanism would operate at intermediate depths.

[49] The second condition is a high degree of hydration on the triggered fault. If faults near the initial rupture are relatively dry, the *P* waves may not reduce the effective normal stress enough for the initial slip (Figure 16c). Adequate hydration is also necessary for the positive feedback mechanism that would cause the second rupture to grow in size. The mechanism by which hydration synchronization occurs may be similar to the stress synchronization described above. If two faults are at different hydration stages, with one fault being well hydrated and the other not at all hydrated, then rupture on the hydrated fault will make water available to the less hydrated fault. This should bring the second fault closer to failure, and bring the rupture cycles of the two faults closer to being in-phase. Both the stress change and hydration mechanisms should act together to bring nearby faults into

synchrony, and may explain why triggering is so common at intermediate depths.

8. Summary

[50] A back projection technique first used by *Ishii et al.* [2005] has been modified for better depth resolution using depth phases, and applied to study the depth-time behavior of 22 intermediate-depth earthquakes recorded at the Hi-net array in Japan. These earthquakes have a variety of magnitudes and source depths. We find that no single subevent has a rupture extent in depth greater than 35 km, and most of the ruptures have vertical extents less than or equal to 15 km. This result supports previous studies that find a prevalence of shallowly dipping rupture planes for large, intermediate-depth earthquakes [e.g., *Suzuki and Kasahara*, 1996; *Delouis and Legrand*, 2007; *Warren et al.*, 2007, 2008]. We, therefore, interpret observations of planes with less than 15 km depth extent as slip on subhorizontal faults created at the outer rise. The frequent occurrence of events with this geometry is explained with preferential focusing of water and subsequent generation of hydrous minerals in subhorizontal faults. The second key observation from this study is that a significant portion of the earthquakes have multiple rupture planes separated in depth. Given the closeness in time and the separation distance of these ruptures, it appears that the seismic waves, specifically, the compressional waves, from one subevent are triggering slip on a different fault. The conditions proposed to explain subhorizontal ruptures also make these faults susceptible to being triggered by seismic waves from an abrupt reduction in the effective normal stress.

[51] **Acknowledgments.** The authors thank the National Research Institute for Earth Science and Disaster Prevention in Japan for making the Hi-net data available. Some figures have been generated using the Generic Mapping Tools [*Wessel and Smith*, 1991]. Discussions with Rachel Abercrombie, Adam M. Dziewoński, Göran Ekström, Amanda Hughes, Peter Kelemen, and James R. Rice helped to test and develop results and concepts in the manuscript. This manuscript also benefitted from constructive reviews by the Associate Editor, Honn Kao, and an anonymous reviewer. This project was funded by NSF EAR-0609092.

References

Allmann, B. P., and P. M. Shearer (2007), A high-frequency secondary event during the 2004 Parkfield earthquake, *Science*, *318*, 1279–1283.

Antolik, M., D. S. Douglas, and B. Romanowicz (1999), Rupture processes of large deep-focus earthquakes from inversion of moment rate functions, *J. Geophys. Res.*, *104*, 863–894.

Baker, T., R. Granat, and R. W. Clayton (2005), Real-time earthquake location using Kirchhoff reconstruction, *Bull. Seismol. Soc. Am.*, *95*, 699–707, doi:101785/0120040123.

Beresnev, I. (2003), Uncertainties in finite-fault slip inversions: To what extent to believe? (a critical review), *Bull. Seismol. Soc. Am. 95*, 2445–2458.

Bergeot, N., M. N. Bouin, M. Diament, B. Pelletier, M. Regnier, S. Calmant, and V. Ballu (2009), Horizontal and vertical interseismic velocity fields in the Vanuatu subduction zone from GPS measurements: Evidence for a central Vanuatu locked zone, *J. Geophys. Res.*, *114*, B06405, doi:10.1029/2007JB005249.

Bevis, M., et al. (1995), Geodetic observations of very rapid convergence and back-arc extension at the Tonga Arc, *Nature*, *374*, 249–251.

Bos, A. G., G. Nolet, A. Rubin, H. Houston, and J. E. Vidale (1998), Duration of deep earthquakes determined by stacking of global seismograph network seismograms, *J. Geophys. Res.*, *103*, 21,059–21,065.

Campus, P., and S. Das (2000), Comparison of the rupture and radiation characteristics of intermediate and deep earthquakes, *J. Geophys. Res.*, *105*, 6177–6189.

Chernak, L. J., and G. Hirth (2010), Deformation of antigorite serpentinite at high temperature and pressure, *Earth Planet. Sci. Lett.*, *296*, 23–33.

Cocco, M., and J. R. Rice (2002), Pore pressure and poroelasticity effects in Coulomb stress analysis of earthquake interactions, *J. Geophys. Res.*, *107*(B2), 2030, doi:10.1029/2000JB000138.

Cohee, B. P., and G. C. Beroza (1994), Slip distribution of the 1992 Landers earthquake and its implications for earthquake source mechanics, *Bull. Seismol. Soc. Am.*, *84*, 692–712.

Cotton, F., and M. Campillo (1995), Frequency domain inversion of strong motions: Application to the 1992 Landers earthquake, *J. Geophys. Res.*, *100*, 3961–3975.

Creager, K. C., and T. M. Boyd (1991), The geometry of Aleutian subduction: Three-dimensional kinematic flow model, *J. Geophys. Res.*, *96*, 2293–2307.

Cruciani, C., E. Carminati, and C. Doglioni (2005), Slab dip vs. lithosphere age: No direct function, *Earth Planet. Sci. Lett.*, *238*, 298–310.

Delouis, B., and D. Legrand (2007), Mw 7.8 Tarapaca intermediate depth earthquake of 13 June 2005 (northern Chile): Fault plane identification and slip distribution by waveform inversion, *Geophys. Res. Lett.*, *34*, L01304, doi:10.1029/2006GL028193.

Dziewonski, A. M., and J. H. Woodhouse (1983), An experiment in systematic study of global seismicity; centroid-moment tensor solutions for 201 moderate and large earthquakes of 1981, *J. Geophys. Res.*, *88*, 3247–3271.

Dziewonski, A. M., T. A. Chou, and J. H. Woodhouse (1981), Determination of earthquake source parameters from waveform data for studies of global and regional seismicity, *J. Geophys. Res.*, *86*, 2825–2852.

Ekström, G. (1994), Anomalous earthquakes on volcano ring-fault structures, *Earth Planet. Sci. Lett.*, *128*, 707–712.

Ekström, G., M. Nettles, and G. Abers (2003), Glacial earthquakes, *Science*, *302*, 622–624.

Ekström, G., A. M. Dziewoński, N. N. Maternovskaya, and M. Nettles (2005), Global seismicity of 2003: Centroid-moment-tensor solutions for 1087 earthquakes, *Phys. Earth Planet. Inter.*, *148*, 327–351.

Flinn, E. A., and E. R. Engdahl (1965), A proposed basis for geographical and seismic regionalization, *Rev. Geophys.*, *3*, 123–149.

Frankel, A. (2004), Rupture process of the M 7.9 Denali Fault, Alaska, earthquake: Subevents, directivity, and scaling of high-frequency ground motions, *Bull. Seismol. Soc. Am.*, *94*, 234–255.

Frohlich, C. (1987), Aftershocks and temporal clustering of deep earthquakes, *J. Geophys. Res.*, *92*, 13,944–13,956.

Frohlich, C. (1989), The nature of deep-focus earthquakes, *Annu. Rev. Earth Planet. Sci.*, *17*, 227–254.

Frohlich, C. (2006), *Deep Earthquakes*, 2nd ed., Cambridge Univ. Press, Cambridge, U. K.

Fromm, R., P. Alvarado, S. L. Beck, and G. Zandt (2006), The April 9, 2001 Juan Fernandez Ridge (Mw 6.7) tensional outer-rise earthquake and its aftershock sequence, *J. Seismol.*, *10*, 163–170.

Green, H. W., II, and P. C. Burnley (1989), A new self-organizing mechanism for deep-focus, *Nature*, *341*, 733–737.

Green, H. W., II, and H. Houston (1995), The mechanics of deep earthquakes, *Annu. Rev. Earth Planet. Sci.*, *23*, 169–213.

Hacker, B. R., S. M. Peacock, G. A. Abers, and S. D. Holloway (2003), Subduction factory: 2. Are intermediate-depth earthquakes in subducting slabs linked to metamorphic dehydration reactions?, *J. Geophys. Res.*, *108*(B1), 2030, doi:10.1029/2001JB001129.

Hartzell, S. H., and T. H. Heaton (1983), Inversion of strong ground motion and teleseismic waveform data for the fault rupture history of the 1979 Imperial Valley, California, earthquake, *Bull. Seismol. Soc. Am.*, *73*, 1553–1583.

Hartzell, S. H., and D. V. Helmberger (1982), Strong-motion modeling of Imperial Valley earthquake of 1979, *Bull. Seismol. Soc. Am.*, *72*, 571–596.

Hino, R., et al. (2009), Insight into complex rupturing of the immature bending normal fault in the outer slope of the Japan Trench from aftershocks of the 2005 Sanriku earthquake (Mw = 7.0) located by ocean bottom seismometry, *Geochem. Geophys. Geosyst.*, *10*, Q07O18, doi:10.1029/2009GC002415.

Hobbs, B. E., and A. Ord (1988), Plastic instabilities: Implications for the origin of intermediate and deep focus earthquakes, *J. Geophys. Res.*, *93*, 10,521–10,540.

Holcombe, C. J. (1977), Earthquake foci distribution in the Sunda arc and the rotation of the backarc area, *Tectonophysics*, *43*, 169–180.

Honda, R., and S. Aoi (2009), Array back projection imaging of the 2007 Niigataken Chuetsu-oki earthquake striking the world's largest nuclear power plant, *Bull. Seismol. Soc. Am.*, *99*, 141–147.

Houston, H. (1993), The non-double-couple component of deep earthquakes and the width of the seismogenic zone, *Geophys. Res. Lett.*, *20*, 1687–1690.

Houston, H. (2001), Influence of depth, focal mechanism, and tectonic setting on the shape and duration of earthquake source time functions, *J. Geophys. Res.*, *106*, 11,137–11,150.
Houston, H., and J. E. Vidale (1994), The temporal distribution of seismic radiation during deep earthquake rupture, *Science*, *265*, 771–774.
Houston, H., H. M. Benz, and J. E. Vidale (1998), Time functions of deep earthquakes from broadband and short-period stacks, *J. Geophys. Res.*, *103*, 29,895–29,913.
Ishii, M., P. M. Shearer, H. Houston, and J. E. Vidale (2005), Extent, duration and speed of the 2004 Sumatra-Andaman earthquake imaged by the Hi-net array, *Nature*, *435*, 933–936.
Ishii, M., P. M. Shearer, H. Houston, and J. E. Vidale (2007), Teleseismic P wave imaging of the 26 December 2004 Sumatra-Andaman and 28 March 2005 Sumatra earthquake ruptures using the Hi-Net array, *J. Geophys. Res.*, *112*, B11307, doi:10.1029/2006JB004700.
Ivandic, M., I. Grevemeyer, J. Bialas, and J. C. Petersen (2010), Serpentinization in the trench-outer rise region offshore of Nicaragua; constraints from seismic refraction and wide-angle data, *Geophys. J. Int.*, *180*, 1253–1264.
Ji, C., D. J. Wald, and D. V. Helmberger (2002), Source description of the 1999 Hector Mine, California, earthquake, part I: Wavelet domain inversion theory and resolution analysis, *Bull. Seismol. Soc. Am.*, *92*, 1192–1207.
Jiao, W., P. G. Silver, Y. Fei, and C. T. Prewitt (2000), Do intermediate- and deep-focus earthquakes occur on preexisting weak zones? An examination of the Tonga subduction zone, *J. Geophys. Res.*, *105*, 28,125–28,138.
Jung, H., H. W. Green, and L. F. Dobrzhinetkaya (2004), Intermediate-depth earthquake faulting by dehydration embrittlement with negative volume change, *Nature*, *428*, 545–549.
Kao, H., and S.-J. Shan (2004), The source-scanning algorithm: Mapping the distribution of seismic sources in time and space, *Geophys. J. Int.*, *157*, 589–594.
Kao, H., and S.-J. Shan (2007), Rapid identification of earthquake rupture plane using source-scanning algorithms, *Geophys. J. Int.*, *168*, 1011–1020.
Kao, H., K. Wang, R.-Y. Chen, I. Wada, J. He, and S.D. Malone (2008), Identifying the rupture plane of the 2001 Nisqually, Washington, earthquake, *Bull. Seismol. Soc. Am.*, *98*, 1546–1558.
Keleman, P. B., and G. Hirth (2007), A periodic shear-heating mechanism for intermediate-depth earthquakes in the mantle, *Nature*, *446*, 787–790.
Kennett, B. L. N. (1991), *IASPEI 1991 Seismological Tables*, Res. Sch. of Earth Sci., Australia Natl. Univ., Canberra, Australia.
Kennett, B. L. N., and E. R. Engdahl (1991), Traveltimes for global earthquake location and phase identification, *Geophys. J. Int.*, *105*, 429–465.
Kirby, S. H., S. Stein, E. A. Okal, and D. C. Rubie (1996), Metastable mantle phase transformations and deep earthquakes in subducting oceanic lithosphere, *Rev. Geophys. 34*, 261–306.
Kobayashi, K., M. Nakanishi, K. Tamaki, and Y. Ogawa (1998), Outer slope faulting associated with the western Kuril and Japan trenches, *Geophys. J. Int.*, *134*, 356–372.
Koulakov, I., and S. V. Sobolev (2006), A tomographic image of Indian lithosphere break-off beneath the Pamir-Hindukush region, *Geophys. J. Int.*, *164*, 425–440.
Kuge, K., Y. Kase, Y. Urata, J. Campos, and A. Perez (2010), Rupture characteristics of the 2005 Tarapaca, northern Chile, intermediate-depth earthquake: Evidence for heterogeneous fluid distribution across the subducting oceanic plate?, *J. Geophys. Res.*, *115*, B09305, doi:10.1029/2009JB007106.
Lay, T., C. J. Ammon, A. R. Hutko, and H. Kanamori (2010), Effects of kinematic constraints on teleseismic finite-source rupture inversion: Great Peruvian earthquakes of 23 June 2001 and 15 August 2007, *Bull. Seismol. Soc. Am.*, *100*, 969–994.
Luyendyk, B. P. (1970), Dips of downgoing lithospheric plates beneath island arcs, *Geol. Soc. Am. Bull.*, *81*, 3411–3416.
MacAyeal, D. R., et al. (2006), Transoceanic wave propagation links iceberg calving margins of Antarctica with storms in tropics and northern hemisphere, *Geophys. Res. Lett.*, *33*, L17502, doi:10.1029/2006GL027235.
Mai, P. M., J. Burjanek, B. Delouis, M. Causse, A. Cirella, G. Festa, C. Francois-Holden, D. Monelli, T. Uchide, and J. Zahradnik (2007), Earthquake source inversion blindtest: Initial results and further developments, *Eos Trans. AGU*, *88*(52), Fall Meet. Suppl., Abstract S53C-08.
Masson, D. G. (1991), Fault patterns at outer trench walls, *Mar. Geophys. Res.*, *13*, 209–225.
McMechan, G. A., J. H. Luetgert, and W. D. Mooney (1985), Imaging of earthquake sources in Long Valley caldera, California, 1983, *Bull. Seismol. Soc. Am.*, *75*, 1005–1020.
Nelson, P., S. Aoi, and F. Hiroyuki (2008), Rupture process of the 2007 Notohanto earthquake by using an isochrones back-projection method and K-NET/KiK-net data, *Earth Planets Space*, *60*, 1035–1040.
Obara, K., K. Kasahara, S. Hori, and Y. Okada (2005), A densely distributed high-sensitivity seismograph network in Japan: Hi-net by National Research Institute for Earth Science and Disaster Prevention, *Rev. Sci. Instrum.*, *76*, 021301, doi:10.1063/1.1854197.
Ogawa, M. (1987), Shear instability in a viscoelastic material as the cause of deep focus earthquakes, *J. Geophys. Res.*, *92*, 13,801–13,810.
Okada, Y., K. Kasahara, S. Hori, K. Obara, S. Sekiguchi, H. Fujiwara, and A. Yamamoto (2004), Recent progress of seismic observation networks in Japan: Hi-net, F-net, K-NET and KiK-net, *Earth Planet. Sci. Lett.*, *56*, 15–28.
Olsen, A. H., and R. J. Apsel (1982), Finite fault and inversion theory with applications to 1979 Imperial Valley earthquake, *Bull. Seismol. Soc. Am.*, *72*, 1969–2001.
Pavlis, G. L., and S. Das (2000), The Pamir-Hindu Kush seismic zone as a strain marker for flow in the upper mantle, *Tectonics*, *19*, 103–115.
Peacock, S. M. (2001), Are the lower planes of double seismic zones caused by serpentine dehydration in subducting oceanic mantle?, *Geology*, *29*, 299–302.
Persh, S. E., and H. Houston (2004), Strongly depth-dependent aftershock production in deep earthquakes, *Bull. Seismol. Soc. Am.*, *94*, 1808–1816.
Raleigh, C. B., and M. S. Paterson (1965), Experimental deformation of serpentinite and its tectonic implications, *J. Geophys. Res.*, *70*, 3965–3985.
Ranero, C., J. P. Morgan, K. McIntosh, and C. Reichert (2003), Bending-related faulting and mantle serpentinization at the Middle American Trench, *Nature*, *425*, 367–373.
Ranero, C., A. Villasenor, J. P. Morgan, and W. Weinrebe (2005), Relationship between bend-faulting at trenches and intermediate-depth seismicity, *Geochem. Geophys. Geosyst.*, *6*, Q12002, doi:10.1029/2005GC000997.
Reitbrock, A., and F. Scherbaum (1994), Acoustic imaging of earthquake sources from the Chalfant Valley, 1985, aftershock series, *Geophys. J. Int.*, *119*, 260–268.
Rhie, J., D. Dreger, R. Bürgmann, and B. Romanowicz (2007), Slip of the 2004 Sumatra-Andaman earthquake from joint inversion of long-period global seismic waveforms and GPS static offsets, *Bull. Seismol. Soc. Am.*, *97*, S115–S127.
Ricker, N. (1953), The form and laws of propagation of seismic wavelets, *Geophysics*, *18*, 10–40.
Ringwood, A. E. (1975), *Composition and Petrology of the Earth's Mantle*, McGraw-Hill, New York.
Romesburg, H. C. (1984), *Cluster Analysis for Researchers*, 334 pp., Lifetime Learn., Belmont, Calif.
Savage, J. C. (1969), The mechanics of deep-focus faulting, *Tectonophysics*, *8*, 115–127.
Schmidt, M. W., and S. Poli (1998), Experimentally based water budgets for dehydrating slabs and consequences for arc magma generation, *Earth Planet. Sci. Lett.*, *163*, 361–379.
Scholz, C. H. (2010), Large earthquake triggering, clustering, and the synchronization of faults, *Bull. Seismol. Soc. Am.*, *100*, 901–909.
Sekiguchi, H., K. Irikura, T. Iwata, Y. Kakehi, and M. Hoshiba (1996), Minute locating of faulting beneath Kobe and the waveform inversion of the source process during the 1995 Hyogo-ken Nanbu, Japan, earthquake using strong ground motion records, *J. Phys. Earth*, *44*, 473–487.
Starovoit, O., S. Yunga, I. Gabsatatova, and L. Chepkunas (2002), Destructive earthquake in Afghanistan (Hindu Kush) on March 25, 2002, *Orfeus Newsl.*, *4*, 11.
Suzuki, S., and M. Kasahara (1996), Unbending and horizontal fracture of the subducting Pacific Plate, as evidenced by the 1993 Kushiro-oki and the 1981 and 1987 intermediate-depth earthquakes in Hokkaido, *Phys. Earth Planet. Inter.*, *93*, 91–104.
Tibi, R., G. Bock, and C. H. Estabrook (2002), Seismic body wave constraint on mechanisms on intermediate-depth earthquakes, *J. Geophys. Res.*, *107*(B3), 2047, doi:10.1029/2001JB000361.
Vidale, J. E., and H. Houston (1993), The depth dependence of earthquake duration and implications for rupture mechanisms, *Nature*, *365*, 45–47.
Wadati, K. (1929), Shallow and deep earthquakes, *Geophys. Mag.*, *2*, 1–36.
Walker, K., and P. M. Shearer (2009), Illuminating the near-sonic rupture velocities of the intracontinental Kokoxili Mw 7.8 and Denali Mw 7.9 strike-slip earthquakes with global P wave back projection imaging, *J. Geophys. Res.*, *114*, B02304, doi:10.1029/2008JB005738.
Walker, K., M. Ishii, and P. M. Shearer (2005), Rupture details of the 28 March 2005 Sumatra Mw 8.6 earthquake imaged with teleseismic *P* waves, *Geophys. Res. Lett.*, *32*, L24303, doi:10.1029/2005GL024395.

Wark, D. A., and E. B. Watson (2000), Effect of grain size on the distribution and transport of deep-seated fluids and melts, *Geophys. Res. Lett.*, *27*, 2029–2032.

Warren, L. M., A. N. Hughes, and P. G. Silver (2007), Earthquake mechanics and deformation in the Tonga-Kermadec subduction zone from fault plane orientations of intermediate- and deep-focus earthquakes, *J. Geophys. Res.*, *112*, B05314, doi:10.1029/2006JB004677.

Warren, L. M., M. A. Langstaff, and P. G. Silver (2008), Fault plane orientations of intermediate-depth earthquakes in the Middle America Trench, *J. Geophys. Res.*, *113*, B01304, doi:10.1029/2007JB005028.

Wessel, P., and W. H. F. Smith (1991), Free software helps map and display data, *Eos Trans. AGU*, *72*, 441.

Woodhouse, J. H., and A. M. Dziewonski (1984), Mapping the upper mantle: Three-dimensional modeling of Earth structure by inversion of seismic waveforms, *J. Geophys. Res.*, *89*, 5953–5986.

Zeng, Y., and J. G. Anderson (1996), A composite source model of the 1994 Northridge earthquake using genetic algorithms, *Bull. Seismol. Soc. Am.*, *86*, S71–S83.

H. Hirose, National Research Institute for Earth Science and Disaster Prevention, 3-1 Tenno-dai, Tsukuba, Ibaraki 305-0006, Japan.

M. Ishii, E. Kiser, and C. H. Langmuir, Department of Earth and Planetary Sciences, Harvard University, 20 Oxford St., Cambridge, MA 02138, USA. (kiser@fas.harvard.edu)

P. M. Shearer, Institute of Geophysics and Planetary Physics, Scripps Institution of Oceanography, IGPP 0225, University of California, San Diego, La Jolla, CA 92093, USA.